Università degli Studi di Roma "Tor Vergata"

FACOLTÀ DI INGEGNERIA

Dipartimento di Informatica Sistemi e Produzione (DISP)

Corso di Dottorato in Geoinformazione - XVII ciclo

Estimation of coniferous vegetation parameters by hyperspectral high spatial resolution satellite images

Simone Cristofori

Relatore:

Prof. Fabio Del Frate

Correlatori:

Dr. Riccardo Benedetti

Dr. Fabio Maselli

keywords: **leaf area index, FAPAR, NDVI, radiative transfer, soil reflectance, CHRIS-PROBA.**

Aprile 2005

Contents

List of Figures

List of Tables

List of Acronyms

AOCS= **A**ttitude **O**rbital **C**ontrol **S**ystem

ASTER= **A**dvanced **S**paceborne **T**hermal **E**mission **R**eflection radiometer

BNSC=**B**ritish **N**ational **S**pace **C**entre

BRF= **B**i-directional **R**eflectance **F**actor

BRDF= **B**i-directional **R**eflectance **D**istribution **F**actor

CHRIS = **C**ompact **H**igh **R**esolution **I**maging **S**pectrometer

CNR= **C**onsiglio **N**azionale delle **R**icerche

CORSARI= **C**luster of **O**ptical **R**emote **S**ensing **A**ctivities **R**esearches and **I**nvestigation

DISORT= **DIS**crete **O**rdinate **R**adiative **T**ransfer

ESA=**E**uropean **S**pace **A**gency

FaPAR = **Fra**ction of **P**hotosynthetically **A**ctive **R**adiation

FWHM= **F**ull **W**idth at **H**alf **M**aximum

GPS= **G**lobal **P**ositioning **S**ystem

IDL= **I**nteractive **D**ata **L**anguage

IFAC=**I**stituto di **F**isica **A**pplicata "Nello **C**arrara"

ISAC=**I**stituto di **S**cienza dell'**A**tmosfera e del **C**lima

JRC=**J**oint **R**esearch **C**enter

LAI = **L**eaf **A**rea **I**ndex

LaMMA= **La**boratorio di **M**eteorologia e **M**odellistica **A**mbientale

LANDSAT= **LAND** remote sensing **SAT**ellite

LUT = **L**ook **U**p **T**able

MERIS= **ME**dium **R**esolution **I**maging **S**pectrometer

MISR= **M**ultiangle **I**maging **S**pectro-**R**adiometer

MODIS= **MOD**erate resolution **I**maging **S**pectroradiometer

MODTRAN= **MOD**erate spectral resolution atmospheric **TRAN**S**m**ittance algorithm

NADIM= **N**ew **A**dvanced **DI**screte **M**odel

NDVI = **N**ormalized **D**ifference **V**egetation **I**dex

NIR = **N**ear **I**nfra**R**ed

NPP= **N**et **P**rimary **P**roductivity

PAI= **P**lant **A**rea **I**ndex

PROBA = **PR**oject for **O**n-**B**oard **A**utonomy

RGB = **R**ed **G**reen **B**lue

RISC= **R**educed **I**nstruction **S**et **C**omputer

SD= **S**tandard **D**eviation

SPIE= The International **S**ociety for O**P**t**I**cal **E**ngineering

SPOT= **S**ysteme **P**our l'**O**bservation de la **T**erre

SZA= **S**olar **Z**enith **A**angle

TOA = **T**op **O**f **A**tmosphere

TOC = **T**op **O**f **C**anopy

Chapter 1

Introduction

Radiative transfer is the most important energy exchange process between the earth-atmosphere system and the rest of the universe (Wallace J.M. and Hobbs P.V., 1977). Top of atmosphere is continually reach by an almost constant solar radiation. Flux of solar energy across a surface of unit area normal to the solar beam at a mean distance between sun and earth is the amount of energy reaching the TOA. It is called **solar constant** and its value is about $1380 W/m^2$ (Liou K.N., 1980).
Solar radiation can be reflected and absorbed by the biosphere components as shown in figure (1.1). By the way, earth emits radiation to space and, over a climatological period of time, earth-atmosphere system is nearly in radiative equilibrium with the sun. The difference from equilibrium force atmospheric and oceanic motions.

Measure of solar radiation reflected by the Earth-Atmosphere system can allows us to extract basic atmospheric and vegetation physical parameters. Atmospheric aerosol affects Earth radiation balance by scattering and absorbing solar radiation and modifying the micro-physical properties of clouds (King M.D., et al, 2003; King M.D. et al, 1999). Estimation of global precipitable water vapor is important to better understand the hydrological cycle, biosphere-atmosphere interaction and for monitoring climate change due to

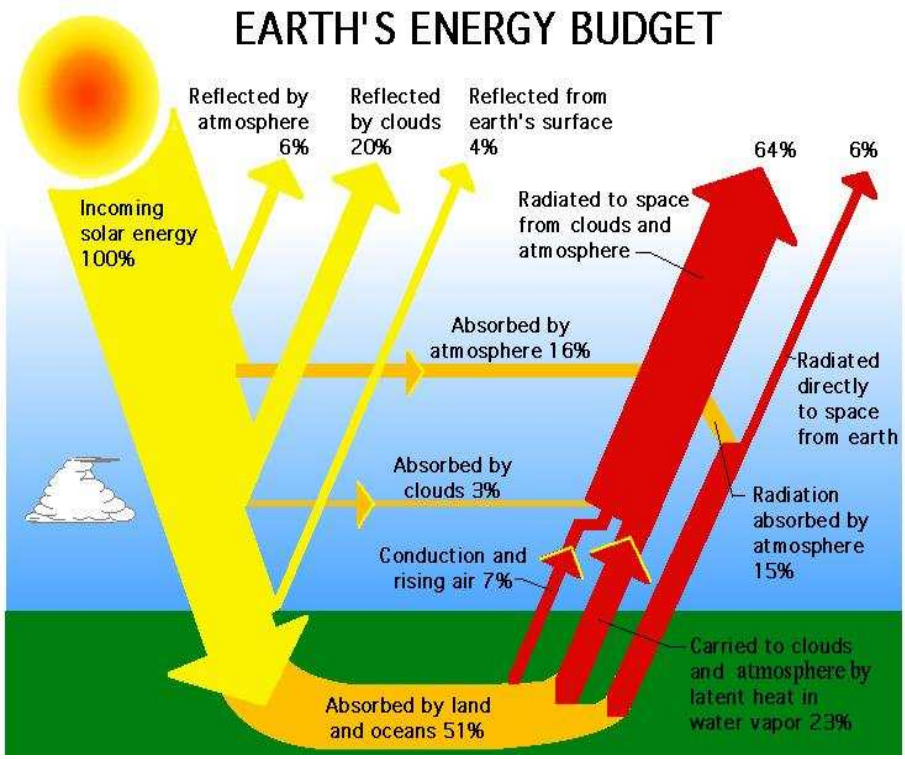

Figure 1.1: *Earth energy balance schematic representation.*

greenhouse gases (Kaufman Y.J. and Gao B., 1992).

Once radiance, measured by an on-board satellite sensor, has been atmospherically corrected can be used to ectract vegetation informations. Leaf area index (LAI) is defined as the one side green leaf area per unit ground area in broadleaf canopies (Myneni R.B, 2002) and as one half the total green leaves area per unit ground area (Benedetti et al., 2005). LAI and Fraction of absorbed (by vegetation) Photosynthetically Active Radiation (FaPAR) are two key parameters to describe many plant processes like evapotranspiration, photosynthesis and, in addition to their effects on radiation exchange with the atmosphere through their effects on albedo (Price J.C. and Bausch, 1995).

Many ecosystem models, like Sim-CYCLE (Hazarika M.K., et al, 2005) BEPS

(Matsushita B. and Tamura M., 2002) use LAI and FaPAR as input parameters to estimate Net Primary Productivity (NPP) o leaf chlorophyll content (Zarco-Tejada et al., 2004). NPP is a key component of terrestrial carbon cycle and it is defined as the net amount of new carbon absorbed by plants per unit of space and time.
For these reasons retrieval LAI and FaPAR from remote sensing data is an active research area.

1.1 Aim of the thesis

The aim of this work is the development and implementation of a new fast and stable algorithm able to create maps of some key vegetation paramenters, which contribute to describe the status of vegetation canopy. The procedure will generate images of retrieved LAI, FaPAR and soil reflectances, in addition to the usual NDVI maps which are immediately calculated by NIR and RED reflectances. Model will analyse data acquired by CHRIS sensor, an experimental hyperspectral high spatial resolution radiometer, on board of PROBA platform. It is reasonably supposed that such analysis will allows us to test the quality and accuracy of images. This is an important aspect for two reasons: the former is that, as previously said, images are acquired by an experimental sensor, which can show distortion in optics, electronic or, simply, in calibration procedure. The latter is that when reflectance data are used to estimate vegetation parameters atmospherical correction algorithms have to be applied in order to have top of canopy reflectances. These algorithms could amplified bias and/or distortions in original data.
The procedure will be devoted to retrieve coniferous vegetation parameters. The choice of this particular biome is the almost total absence of a data-base of single needle physical and geometrical properties, which are needed for the vegetation radiative transfer problem solution (Kuusk, A. and Nilson T.,

2000, Gobron N., et al., 1997). Then it is useful to describe needle as better as possible. LOPEX 2003 (Hosgood b., et al., 2003) is one of the most used vegetation spectral characteristics data-base. It provides measures acquired on a large number of canopy types. Broad leaf species are well and accurately described, while coniferous properties are measured on a compressed pastille of a large number of needles. It is obviuos that this is a too strong and unrealistic approximation of needle-leaves spectral characteristics.
In the last years, in the framework of BOREAS project, a new radiative transfer model and spectral data-base for coniferous canopy is under development (Hu B., et al., 2004; Zarco-Teiada P.J., et al., 2004). For these reasons, in this work, laboratory acquisitions will aim at extracting single leaf properties of maritime or domestic pine. As single vegetation element we will consider little pine branches, with a low number of pine shoots. Reflectances and destructive LAI measurements will give us the possibility to estimate "single leaf" properties, like extinction coefficient and reflectance of infinitely thick canopy, then used as input in the retrieval model. This model will be based on the two fluxes approximation.
Finally, once LAI, soil reflectances and FaPAR results are validated they can be used in other algorithms to estimate NPP or as input of climate and large scale ecosystem model (Wang Y., et al, 2004).

1.2 Organization of dissertation

The current thesis is divided into six chapters:
Chapter 1: The introduction (this one).

Chapter 2: in this chapter the basic definitions and theory of the radiative transfer will be summarized. Particularly will be pointed out the Bidirectional Reflectance Distrubution Function definition and the mathemati-

cal description of the two fluxes approximation. Introduction of illumination and viewing direction illumination allow us a more detailed treatment of the problem as describe in Appendix A.

Chapter 3: in this chapter the main characteristics of the instruments used will be reported. CHRIS sensor gives us the spectral images on the San Rossore test site, as used to extract the vegetation parameters. Portable spectroradiometer SPEC-PRO is used to measure ground based and laboratory canopy reflectances. Li-Cor LAI2000 allows us to measure in-situ vegetation canopy LAI.

Chapter 4: here LAI, canopy and soil reflectances measurements on San Rossore test site and Florence laboratory will be described. Measures on San Rossore allow us to estimate validation parameters. By the way, using laboratory measurements we obtain the vegetation parameters to feed the retrieval algorithm.

Chapter 5: CHRIS data processing will be describe in this chapter. LAI, fAPAR and soil reflectance retrieval algorithms have been developed starting from the two fluxes approximation described in chapter 2 and the soil line extraction from CHRIS RED and NIR images. From laboratory measurements we obtain canopy scattering coefficients and infinitely thick canopy reflectance to insert into the LAI retrieval algorithm.

Chapter 6: in this chapter results obtained from CHRIS images analysis, by means of retrieval algorithms described in chapter 5, will be summarized. Moreover validation processes, conclusion and future plans will be presented. In addition to these six chapters two appendices are included. The former is for the four streams approximation mathematical approach we aim at im-

plementing as future work. The latter is to show the bad quality of spectral channel 17 CHRIS images.

Chapter 2

Radiative transfer

2.1 Introduction

Radiative transfer is the most important process in the energy transfer between the earth-atmosphere system and the rest of the universe.
Before dealing with the specific application and the experimental work let us summarize the basic definition and the radiative transfer theory which the followed approach is founded on.

2.2 Specific intensity, net flux and Lambertian surface

Let dE_ν denote the amount of radiant energy in the frequency interval $(\nu, \nu + d\nu)$ which flows, during the time interval $(t, t + dt)$, through the surface element $d\sigma$ and within the solid angle element $d\Omega_{\hat{s}}$ about the $\hat{\boldsymbol{s}}$ direction. It is often convenient to express this radiant energy in terms of the *specific intensity*, or *intensity* "tout-court", $I_{\hat{s}}$ by:

$$dE_\nu = (\hat{\boldsymbol{s}} \cdot \hat{\boldsymbol{n}}) I_{\hat{s}} d\sigma d\Omega_{\hat{s}} d\nu dt \tag{2.1}$$

where $\hat{\boldsymbol{n}}$ denotes the outward normal versor to $d\sigma$. In plane words $I_{\hat{s}}(\boldsymbol{r}, \nu, t)$ represents the radiant energy per unit surface, solid angle, frequency and time

flowing through the $\boldsymbol{r}$-located surface element $d\sigma$ whose normal versor $\hat{\boldsymbol{n}}$ is parallel to $\hat{\boldsymbol{s}}$, so that $\hat{\boldsymbol{s}} \cdot \hat{\boldsymbol{n}}$=1. Notice that for a perfectly collimated radiation in $\hat{\boldsymbol{s}}$ direction, the specific intensity is a delta-function of the solid angle, i.e. $I_{\hat{s}} = \mathcal{I}_0 \delta(\Omega - \Omega_{\hat{s}})$, where $\mathcal{I}_0$ stands for the usual radiation intensity (energy per unit area, time and frequency passing through a surface perpendicular to the propagation direction $\hat{\boldsymbol{s}}$). The geometrical construction used for defining $I_{\hat{s}}$ and represented in fig.2.1.a also defines a *pencil of radiation*. If the specific intensity at a given point does not depend on the direction $\hat{\boldsymbol{s}}$ the radiation field is said to be *isotropic* at that point. Besides if the intensity remains the same at all the spatial points $\boldsymbol{r}$, the field is said *homogeneous*.

The quantity:

$$\pi F \equiv \int_{4\pi} (\hat{\boldsymbol{s}} \cdot \hat{\boldsymbol{n}}) I_{\hat{s}} d\Omega_{\hat{s}} \tag{2.2}$$

where the integration is performed all over the solid angle centred in $d\sigma$ position $\boldsymbol{r}$, is called *net flux* and indicates the radiant power flowing per unit area and frequency interval through $d\sigma$. The constant π enters the net flux definition just by common consent due to the fact that for a surface emitting a constant specific intensity I_0 into any outward direction $\hat{\boldsymbol{s}}$[1] and nought elsewhere, the value π is the result of the merely geometrical integral:

$$\int_{2\pi^+} \hat{\boldsymbol{s}} \cdot \hat{\boldsymbol{n}} d\Omega_{\hat{s}} = \int_0^{2\pi} d\phi_{\hat{s}} \int_0^{\frac{\pi}{2}} \cos\theta_{\hat{s}} \sin\theta_{\hat{s}} d\theta_{\hat{s}} = \pi \tag{2.3}$$

Thus for such one-sided surface, known as *Lambertian*, the quantity F exactly corresponds to its specific intensity I_0 emitted in any direction. Differently for a generic emitting surface, F denotes the equivalent specific intensity one has to assign to an identical (in geometrical sense) but Lambertian surface for obtaining the same net flux.

Clearly F depends on the orientation $\hat{\boldsymbol{n}}$ of the elementary surface through which the net flux is evaluated. However its dependence is vector-like. For

[1] That is into the "upward" hemisphere $2\pi^+$ for which $\hat{\boldsymbol{s}} \cdot \hat{\boldsymbol{n}} \geq 0$.

instance considering an orthogonal triplet $\hat{\boldsymbol{x}}$, $\hat{\boldsymbol{y}}$, $\hat{\boldsymbol{z}}$ if $\hat{\boldsymbol{n}} = l\hat{\boldsymbol{x}} + m\hat{\boldsymbol{y}} + n\hat{\boldsymbol{z}}$, then:

$$F(\hat{\boldsymbol{n}}) = lF(\hat{\boldsymbol{x}}) + mF(\hat{\boldsymbol{y}}) + nF(\hat{\boldsymbol{z}}) \tag{2.4}$$

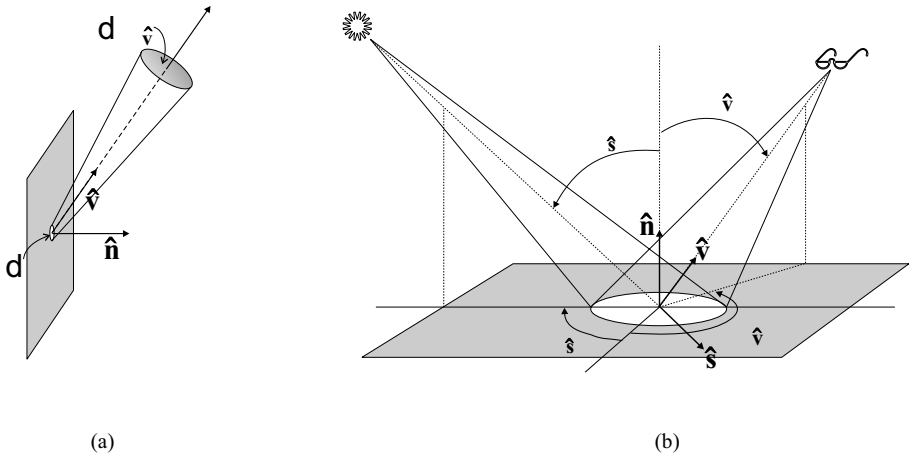

(a) (b)

Figure 2.1: *(a) Geometrical construction for defining the specific intensity and (b) illumination and viewing geometry for BRDF definition.*

2.3 The Bi-directional Reflectance Distribution Function

It frequently happens to have something to do with the radiation reflected by a surface under specific conditions of illumination. Let us suppose the surface element $d\sigma$ is illuminated only by the pencil of radiation $I_{\hat{s}}$. The simplest hypothesis, valid for the most cases of interest, consists in assuming the specific intensity $I_{\hat{v}}$ reflected by $d\sigma$ in $\hat{\boldsymbol{v}}$ direction proportional to the incidend flux $\pi F_{\hat{s}} = |\hat{\boldsymbol{s}} \cdot \hat{\boldsymbol{n}}| I_{\hat{s}} d\Omega_{\hat{s}}$:

$$I_{\hat{v}} = \varrho(\hat{\boldsymbol{s}}, \hat{\boldsymbol{v}}) |\hat{\boldsymbol{s}} \cdot \hat{\boldsymbol{n}}| I_{\hat{s}}\, d\Omega_{\hat{s}} \tag{2.5}$$

The geometrical[2] function $\varrho(\hat{\boldsymbol{s}}, \hat{\boldsymbol{v}})$ is known as *Bi-directional Reflectance Distribution Function*, in short BRDF, and it allows to determine the reflected

[2] As obvious ϱ also depends on the features of the surface and the frequency of the radiation, but not on the incident intensity.

specific intensity once the illuminating radiation is given. When such radiation arrives on $d\sigma$ from more directions an integration of the right hand term in 2.5 all over the "upwards" hemisphere is required:

$$I_{\hat{v}} = \int_{2\pi^+} \varrho(\hat{\boldsymbol{s}}', \hat{\boldsymbol{v}}) |\hat{\boldsymbol{s}}' \cdot \hat{\boldsymbol{n}}| I_{\hat{s}'} \, d\Omega_{\hat{s}'} \tag{2.6}$$

Hence for a perfectly collimated radiation in $\hat{\boldsymbol{s}}$ direction of intensity $\mathcal{I}_0$ the following relation holds:

$$I_{\hat{v}} = \varrho(\hat{\boldsymbol{s}}, \hat{\boldsymbol{v}}) |\hat{\boldsymbol{s}} \cdot \hat{\boldsymbol{n}}| \mathcal{I}_0 \tag{2.7}$$

The BRDF of a Lambertian surface reflecting, on the whole, a fraction r of the incident radiation all over the "upward" hemisphere has the very simple form:

$$\varrho_L = \frac{r}{\pi} \tag{2.8}$$

Clearly this result comes directly from the fact that, by definition of Lambertian surface, the reflected specific intensity does not depend on the viewing direction and its integral over the entire "upward" hemisphere has to equal the fraction r of incident flux $\pi F_{\hat{s}}$.

It frequently happens that the BRDF of a generic surface is normalized to the one of a perfectly reflecting ($r = 1$) Lambertian surface under identical condition of illumination and instead of $\varrho(\hat{\boldsymbol{s}}, \hat{\boldsymbol{v}})$ the *Bi-directional Reflectance Factor*, in short BRF, is given:

$$\hat{\varrho}(\hat{\boldsymbol{s}}, \hat{\boldsymbol{v}}) \equiv \pi \varrho(\hat{\boldsymbol{s}}, \hat{\boldsymbol{v}}) \tag{2.9}$$

From an operational point of view the BRDF is determined by illuminating the surface with a known intensity $I_{\hat{s}} d\Omega_{\hat{s}}$ of well collimated radiation and hence measuring the radiant intensity $\mathcal{I}_{\hat{v}}(\boldsymbol{r}+R\hat{\boldsymbol{v}})$ impinging on a detector surface da placed in $\hat{\boldsymbol{v}}$ direction at large distance R from the $\boldsymbol{r}$-located $d\sigma$. Once the optical apparatus of the detector is focused on the target $d\sigma$, it

collects radiation confined to the solid angle element $\frac{d\sigma}{R^2}\ (\hat{\boldsymbol{n}} \cdot \hat{\boldsymbol{v}})$ about $\hat{\boldsymbol{v}}$, as shown in fig.2.2a. Since da is viewed from $d\sigma$ under the solid angle $\frac{da}{R^2}$, the measured energy rate arriving on da results[3]:

$$\mathcal{I}_{\hat{v}}(\boldsymbol{r} + R\hat{\boldsymbol{v}})da = I_{\hat{v}}(\boldsymbol{r})\ \hat{\boldsymbol{n}} \cdot \hat{\boldsymbol{v}}\ d\sigma \frac{da}{R^2} \tag{2.10}$$

and the BRDF can be calculated according to its definition 2.5.

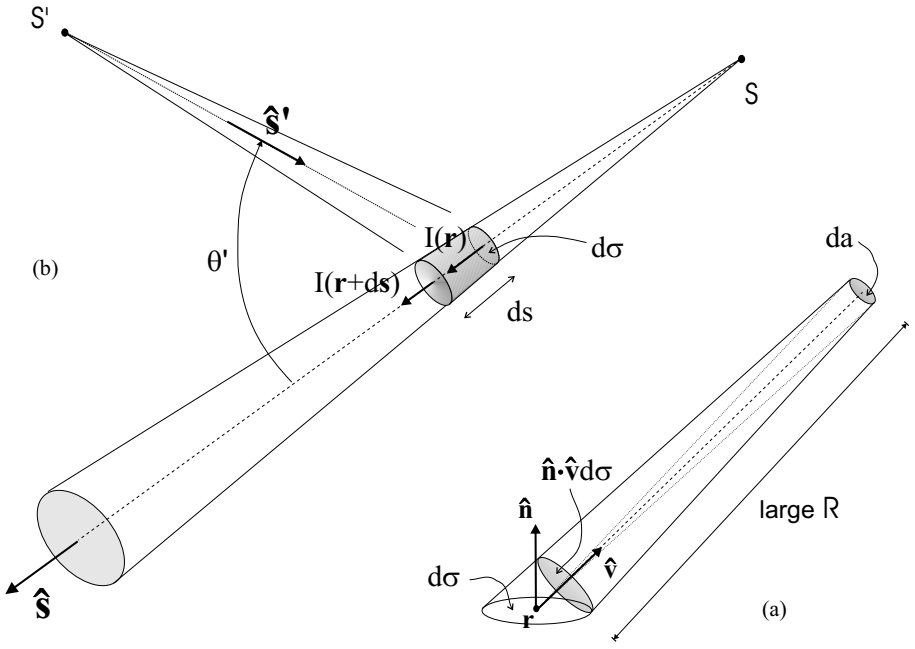

Figure 2.2: *(a) Schematic draw of the BRDF determination and (b) representation of the scattering geometry by the volume dV considered for writing the radiative transfer equation.*

2.4 Radiative transfer in turbid media

When a single pencil of radiation traverses matter of density ρ for a thickness ds into the direction $\hat{\boldsymbol{s}}$ of its propagation, the intensity $I_{\hat{s}}$ decreases by the amount:

$$dI_{\hat{s}} \equiv I_{\hat{s}}(\boldsymbol{r} + ds\hat{\boldsymbol{s}}) - I_{\hat{s}}(\boldsymbol{r}) = -\kappa_e \rho I_{\hat{s}}(\boldsymbol{r})ds \tag{2.11}$$

[3]Here we suppose the medium between da and $d\sigma$ perfectly transparent. Otherwise a contribution due to both scattering and absorption of intervening matter is present.

The quantity $\kappa_e = \kappa_e(\nu)$ defines the *mass extinction coefficient* for radiation of frequency ν. It depends only on the kind of material and accounts for all the possible interactions radiation-matter which modify the intensity $I_{\hat{s}}$, both as a consequence of *true absorption*, i.e. conversion of radiant energy in different forms of energy or radiant energy of different frequency, and *elastic scattering*, i.e. photons deflected without any change of their frequency. For this reason is often useful to distinguish between a true absorption coefficient κ_a and a scattering coefficient κ_s writing $\kappa_e = \kappa_a + \kappa_s$. In many cases such a distinction is made in terms of the absorption and scattering cross sections σ_a and σ_s, defined as the geometrical cross sections one has to assign to each scatterer particle (atom, molecule or aggregate) for making the fractions of surface covered by the particles in the layer of thickness ds equal to the fractions $\kappa_a \rho\ ds$ and $\kappa_s \rho\ ds$ of absorbed and scattered intensity. Since for a number N of scatterers per unit volume the fraction of covered surface turns out to be $N\sigma_e ds \equiv N(\sigma_a + \sigma_s)ds$, the relationships between mass coefficients and cross sections are:

$$\kappa_a \rho = N\sigma_a \quad \text{and} \quad \kappa_s \rho = N\sigma_s \quad \Rightarrow \quad \kappa_e \rho = N\sigma_e \tag{2.12}$$

The whole fraction of energy scattered in elastic way out of the total removed from the pencil of radiation according to 2.11 is called *single scattering albedo*[4] w_0 and it clearly corresponds to the ratio $\frac{\kappa_s}{\kappa_e} = \frac{\sigma_s}{\sigma_e}$. In order to describe quantitatively such elastic processes an angular distribution of the scattered radiation is also needed. Therefore the *single scattering phase*

[4]The name "single scattering" obviously comes from the fact that the large part of the photons scattered by the volume element $dV = d\sigma\ ds$ suffered only one scattering event. This determines the criterium for quantifying both the infinitesimal size of dV and the limit of validity for the treatment in terms of single particle cross sections and single scattering events. In particular ds has to be much smaller than the mean free photon path $\frac{1}{N\sigma_e}$ and the area $d\sigma$ larger than σ_e but much smaller than the square of the mean photon path. These conditions necessarily imply that $\sqrt[3]{\frac{1}{N}} \gg \sigma_e$, thus fixing an upper limit to the volume density of particles N for the validity of the single scattering approach.

function $p_0(\hat{\boldsymbol{s}},\hat{\boldsymbol{v}})$ is introduced. By definition it represents the probability per solid angle fraction of finding a scattered photon in $\hat{\boldsymbol{v}}$ direction and, as obvious, it is normalized to unit all over the solid angle centred at the scatterer volume dV:

$$\int_{4\pi} p_0(\hat{\boldsymbol{s}},\hat{\boldsymbol{v}})\,\frac{d\Omega_{\hat{v}}}{4\pi} = 1 \tag{2.13}$$

From an operational point of view the phase function 2.13 is determined by measuring the scattered radiant intensity $\mathcal{I}_{\hat{v}}\,(\boldsymbol{r}+R\hat{\boldsymbol{v}})$ that reachs the sensitive area da of a detector placed at large distance $R \gg \sqrt{d\sigma}$ from the $\boldsymbol{r}$-located volume dV:

$$\frac{1}{4\pi}p_0(\hat{\boldsymbol{s}},\hat{\boldsymbol{v}}) = \frac{\mathcal{I}_{\hat{v}}(\boldsymbol{r}+R\hat{\boldsymbol{v}})}{\displaystyle\int_{4\pi}\mathcal{I}_{\hat{v}'}(\boldsymbol{r}+R\hat{\boldsymbol{v}}')\,d\Omega_{\hat{v}'}} \tag{2.14}$$

Clearly the integral at denominator in 2.14 multiplied by R^2 gives the total energy per unit frequency and time scattered in elastic way by $dV = d\sigma ds$, i.e. $w_0\kappa_e I_{\hat{s}}\,(\boldsymbol{r})d\Omega_{\hat{s}}\rho\; d\sigma ds$. Thus the scattered intensity in $\hat{\boldsymbol{v}}$ direction at distance R from the $\boldsymbol{r}$-located mass element $dm \equiv \rho d\sigma ds$ may be expressed in terms of the specific intensity $I_{\hat{s}}(\boldsymbol{r})$ incident on dm as:

$$\mathcal{I}_{\hat{v}}(\boldsymbol{r}+R\hat{\boldsymbol{v}}) = \frac{1}{4\pi R^2}\,w_0\kappa_e I_{\hat{s}}(\boldsymbol{r})d\Omega_{\hat{s}}dm\;p_0(\hat{\boldsymbol{s}},\hat{\boldsymbol{v}}) \tag{2.15}$$

This expression tells us the mass element dm behaves, at large distance, as a point-like source emitting a total amount of energy at rate $w_0\kappa_e I_{\hat{s}}(\boldsymbol{r})d\Omega_{\hat{s}}dm$ angularly modulated by the phase function $p_0(\hat{\boldsymbol{s}},\hat{\boldsymbol{v}})$, whose value for isotropic scattering is obviously constant and equal to 1.

2.4.1 The radiative transfer equation

When only a single pencil of radiation in $\hat{\boldsymbol{s}}$ direction is present, the equation of transfer for its passage through an isolated mass element dm is given by 2.11. On the contrary if dm is illuminated from different directions $\hat{\boldsymbol{s}}'$, as occurs when more point-like sources are present and/or the illuminated

volume has finite size, the net result for the variation of specific intensity in $\hat{\boldsymbol{s}}$ direction includes not only the absorption along the thickness ds but also the scattering from $\hat{\boldsymbol{s}}'$ to $\hat{\boldsymbol{s}}$ by dm. The detailed account of this contribution becomes possible under some conditions. When the number N of scatterer particles per unit volume is sufficiently low the photon mean free path in the medium, $\frac{1}{N\sigma_e}$, becomes large enough for considering each particle like a point when viewed from its nearest scatterer neighbour. As known a light source cannot be localized in a volume of linear dimension smaller than the wavelength λ of the emitted radiation. Thus for particles with radius r_p of the same order of λ or smaller, the following relation must be satisfied:

$$\frac{1}{N\sigma_e} \gg \lambda \qquad \text{when} \qquad \lambda \gtrsim r_p \tag{2.16}$$

When we have particles much larger than the wavelength, i.e. $r_p \gg \lambda$, a more restrictive condition is required in order to avoid shadows between neighbouring particles. As known from geometrical optics the casting of shadows with fairly sharp outline of the same shape as the illuminated object is ruled by Fresnel diffraction[5]. When the dimension of the object is so small and its distances, d_s from the source and d_o from the observing screen, so large that the number n of Fresnel zones covered by the object is sufficiently low, then no any shadow is formed. Since the radius r_n of the n-th Fresnel zone is such that:

$$r_n^2 = n\lambda \frac{d_s d_o}{d_s + d_o} \tag{2.17}$$

taking the photon mean free path $\frac{1}{N\sigma_e}$ as distance from the screen with source at infinite[6] the sought condition for particles of mean radius r_p turns out to be:

$$\frac{1}{N\sigma_e} \geq \frac{r_p^2}{n\lambda} \qquad \text{when} \quad r_p \gg \lambda \tag{2.18}$$

[5]Fresnel diffraction occurs when either the source of light or the observing screen, or both, are at finite distance from the diffracting object.

[6]That is $d_s \to \infty$. This means we consider a perfectly collimated radiation, a more restrictive condition than the one following from the assumption of source placed at the same distance than the screen.

which also implies $\frac{1}{N\sigma_e} \gg r_p$, analogously to 2.16. When the conditions 2.16 or 2.18 are satisfied each element of volume dV that composes the medium behaves like it would be isolated with a constant illumination all over every surface of the order of $d\sigma$[7]. Hence the contribution to the specific intensity $I_{\hat{s}}$ due to the scattering of radiation travelling for a thickness ds in $\hat{\boldsymbol{s}}'$ direction can be written as:

$$w_0 \kappa_e \rho I_{\hat{s}'} ds \, p_0(\hat{\boldsymbol{s}}', \hat{\boldsymbol{s}}) \frac{d\Omega_{\hat{s}'}}{4\pi} \tag{2.19}$$

Therefore the equation of transfer when only absorption and elastic scattering are present takes the form:

$$dI_{\hat{s}} = -\kappa_e \rho I_{\hat{s}} ds + \left[\int_{4\pi} w_0 \kappa_e \rho I_{\hat{s}'} p_0(\hat{\boldsymbol{s}}', \hat{\boldsymbol{s}}) \frac{d\Omega_{\hat{s}'}}{4\pi} \right] ds \tag{2.20}$$

For a general formulation it is convenient to introduce the *emission coefficient* $j_{\hat{s}}$ so that the amount of radiant energy dE_ν^{em} emitted by the element of mass dm in the frequency interval $(\nu, \nu + d\nu)$, in time dt and confined to the solid angle $d\Omega_{\hat{s}}$ about the $\hat{\boldsymbol{s}}$ direction is given by:

$$dE_\nu^{\mathrm{em}} = j_{\hat{s}} dm d\Omega_{\hat{s}} d\nu dt \tag{2.21}$$

It should be noted that the emission coefficient as defined above accounts for the radiation emitted by dm without any regard of its physical generation process. Thus it includes both radiation scattered in elastic or inelastic way and radiation coming from "true" emission, such as the one due to thermal emission. In any case the change in the radiant energy crossing normally the two faces $d\sigma$ of the volume $dV \equiv ds d\sigma = \frac{dm}{\rho}$ within the solid angle element $d\Omega_{\hat{s}}$ and expressed by:

$$\frac{dI_{\hat{s}}}{ds} ds d\sigma d\Omega_{\hat{s}} d\nu dt \tag{2.22}$$

must arise from the difference between emission and absorption in the frequency interval and element of solid angle considered. Since the amount of

[7] This obviously breaks down when shadows are present.

absorbed radiant energy is $\kappa_e \rho I_{\hat{s}} ds d\sigma d\Omega_{\hat{s}} d\nu dt$ while the amount emitted is $j_{\hat{s}} \rho ds d\sigma d\Omega_{\hat{s}} d\nu dt$, the total budget based on the conservation principle immediately gives the general expression of the radiative transfer equation:

$$\frac{dI_{\hat{s}}}{ds} = -\kappa_e \rho I_{\hat{s}} + \rho j_{\hat{s}} \tag{2.23}$$

or, being the left hand side term the directional derivative along $\hat{\boldsymbol{s}}$,:

$$\frac{1}{\kappa_e \rho} \hat{\boldsymbol{s}} \cdot \boldsymbol{\nabla} I_{\hat{s}}(\boldsymbol{r}) = -I_{\hat{s}}(\boldsymbol{r}) + \frac{j_{\hat{s}}(\boldsymbol{r})}{\kappa_e} \tag{2.24}$$

where the ratio $j_{\hat{s}}/\kappa_e$ of the emission to the extinction coefficient is called *source function*. The formal solution of 2.24 can be readily written down:

$$I_{\hat{s}}(\boldsymbol{r}_0 + s\hat{\boldsymbol{s}}) = I_{\hat{s}}(\boldsymbol{r}_0) e^{-\tau_{\hat{s}}(\boldsymbol{r}_0, s)} + \int_0^s \rho j_{\hat{s}}(\boldsymbol{r}_0 + \xi \hat{\boldsymbol{s}}) e^{\tau_{\hat{s}}(\boldsymbol{r}_0 + \xi \hat{\boldsymbol{s}}, s-\xi)} d\xi \tag{2.25}$$

where $\tau_{\hat{s}}(\boldsymbol{r}, s)$ is the *optical thickness* of the medium between the points $\boldsymbol{r}$ and $\boldsymbol{r} + s\hat{\boldsymbol{s}}$:

$$\tau_{\hat{s}}(\boldsymbol{r}, s) \equiv \int_0^s \kappa_e(\boldsymbol{r} + \xi \hat{\boldsymbol{s}})\, \rho(\boldsymbol{r} + \xi \hat{\boldsymbol{s}})\, d\xi \tag{2.26}$$

and $\boldsymbol{r}_0$ denotes a generic point where the specific intensity is known. It is important to remark that 2.25 only represents a formal solution which simply tells us that the specific intensity at any point s away from $\boldsymbol{r}_0$ in a given direction $\hat{\boldsymbol{s}}$ results from the emission at all anterior points $\boldsymbol{r}_0 + \xi \hat{\boldsymbol{s}}$ reduced by the factor $e^{-\tau_{\hat{s}}(\mathbf{r}_0 + \xi \hat{\mathbf{s}}, s-\xi)}$ due to the absorption by intervening matter.

Any attempt to solve in a real sense the radiative transfer equation 2.24 requires both an explicit expression of the source function and boundary conditions for the specific intensity. For example in the case of scattering atmosphere the source function, as stated by eqn.2.20, is:

$$\frac{j_{\hat{s}}}{\kappa_e} = w_0 \int_{4\pi} I_{\hat{s}'}\, p_0(\hat{\boldsymbol{s}}', \hat{\boldsymbol{s}})\, \frac{d\Omega_{\hat{s}'}}{4\pi} \tag{2.27}$$

while the boundary conditions with the assumption of illumination by perfectly collimated radiation of intensity $\mathcal{I}_{\hat{s}}$ and dark soil[8] are given by:

$$\begin{aligned} I_{\hat{s}'}(\boldsymbol{r},\nu,t) &= \mathcal{I}_{\hat{s}}(\hat{\boldsymbol{s}},\nu,t)\,\delta(\Omega_{\hat{s}'}-\Omega_{\hat{s}}) \qquad \text{for } \boldsymbol{r}\in S_{\text{TOA}} \\ I_{\hat{s}'}(\boldsymbol{r},\nu,t) &= 0 \qquad\qquad \text{for } \boldsymbol{r}\in S_{\text{soil}} \end{aligned} \tag{2.28}$$

where $\hat{\boldsymbol{s}}'$ denotes a generic inward (into atmosphere) direction and S_{TOA}, S_{soil} are the boundary surfaces at top of atmosphere and soil, respectively.

2.5 The two streams approximation

Let us consider a z-oriented parallel planes medium with optical thickness τ in z direction. The two streams approximation consists in writing down two coupled differential equations for the net downwelling ($_+$) and upwelling ($_-$) fluxes $F_\pm$, defined by integration of the specific intensity all over the upward (Ω_-) and downward (Ω_+) hemisphere:

$$F_\pm = \int_{\Omega_\pm} |\hat{\mathbf{s}}\cdot\hat{\mathbf{z}}| I_{\hat{\mathbf{s}}} d\Omega_{\hat{\mathbf{s}}} \tag{2.29}$$

where $\hat{\mathbf{z}}$ denotes the normal versor to the symmetry planes. For an infinitesimal thickness $d\tau$ of the medium a fraction $\hat{k}_+F_+$ of the downwelling flux is absorbed while a fraction $\hat{\sigma}_+F_+$ is backscattered in upward direction to enforce the upwelling flux. Since the same occurs for the flux F_-, the system of two differential equation for the total radiation budget can be easily written as:

$$\begin{cases} \dfrac{dF_+}{d\tau} = -\hat{k}_+F_+ + \hat{\sigma}_-F_- \\ \dfrac{dF_-}{d\tau} = -\hat{\sigma}_+F_+ + \hat{k}_-F_- \end{cases} \tag{2.30}$$

or, in matricial form:

$$\frac{d\boldsymbol{F}}{d\tau} = \mathbb{S}\boldsymbol{F} \tag{2.31}$$

[8] That is a perfectly absorbing soil with a negligible thermal emission at the wavelength considered.

where:

$$\boldsymbol{F} = \begin{pmatrix} F_+ \\ F_- \end{pmatrix} \qquad \text{and} \qquad \mathbb{S} = \begin{pmatrix} -\hat{k}_+ & \hat{\sigma}_- \\ -\hat{\sigma}_+ & \hat{k}_- \end{pmatrix} \tag{2.32}$$

If $\hat{\mathbf{e}}_1$ and $\hat{\mathbf{e}}_2$ are two eigenvectors of the scattering matrix with eigenvalues $\hat{\alpha}_1$ and $\hat{\alpha}_2$, respectively, any solution can be written as:

$$\boldsymbol{F} = F_1\hat{\mathbf{e}}_1 + F_2\hat{\mathbf{e}}_2 \tag{2.33}$$

By substitution in eqn.2.31 we get:

$$\frac{dF_i}{d\tau} = \hat{\alpha}_i F_i \qquad i = 1, 2 \tag{2.34}$$

whose solutions are clearly:

$$F_i(\tau) = F_i(0)e^{\hat{\alpha}_i\tau} \qquad i = 1, 2 \tag{2.35}$$

This means that the searched solutions $F_\pm(\tau)$ must be of the form:

$$F_\pm(\tau) = \sum_{i=1}^{2} c_{i\pm} e^{\hat{\alpha}_i\tau} \tag{2.36}$$

where $c_{i\pm}$ are coefficients independent of τ whose value is determined requiring that system 2.30 is satisfied by the two exponential solutions independently (two conditions) and by imposing the boundary conditions (two other conditions, for example at the top and at the bottom of the medium). In particular by substituting the exponential terms of 2.36 in 2.30 we get the characteristic equation to find the eigenvalues $\hat{\alpha}_i$ as well as the relations between c_- and c_+ coefficients:

$$\begin{aligned} &\left[(\hat{\alpha}_i + \hat{k}_+)(\hat{\alpha}_i - \hat{k}_-) + \hat{\sigma}_+\hat{\sigma}_-\right] = 0 \\ &c_{i-} = r_i c_{i+} \qquad \text{with} \qquad r_i = \frac{\hat{\sigma}_+}{(\hat{k}_- - \hat{\alpha}_i)} = \frac{(\hat{k}_+ + \hat{\alpha}_i)}{\hat{\sigma}_-} \end{aligned} \tag{2.37}$$

The two eigenvalues $\hat{\alpha}_1$ and $\hat{\alpha}_2$ of the scattering matrix $\mathbb{S}$ are:

$$\begin{aligned}\hat{\alpha}_1 &= \frac{(\hat{k}_+ - \hat{k}_-) - \sqrt{(\hat{k}_+ + \hat{k}_-)^2 - 4\hat{\sigma}_+\hat{\sigma}_-}}{2} \\ \hat{\alpha}_2 &= \frac{(\hat{k}_+ - \hat{k}_-) + \sqrt{(\hat{k}_+ + \hat{k}_-)^2 - 4\hat{\sigma}_+\hat{\sigma}_-}}{2}\end{aligned} \tag{2.38}$$

It is important to notice that for passive medium the energy conservation requires that $0 \leq \hat{\sigma}_\mp \leq \hat{k}_\mp \leq 1$. These relations imply opposite signs for the scattering matrix eigenvalues, namely $\hat{\alpha}_1 \leq 0$ and $\hat{\alpha}_2 \geq 0$. The two remaining coefficients c_{i+} are finally determined by the boundary conditions. Let us consider the typical situation of a given incident radiation F_0 at the top of the medium ($\tau = 0$) with an underlying Lambertian surface of reflectance r_s at $\tau = T$. In this case the boundary conditions read $F_+(\tau) = F_0$ and $F_-(T) = r_s F_+(T)$ and taking the expressions 2.36 we get the system:

$$\begin{cases} c_{1+} + c_{2+} = F_0 \\ \\ (r_1 - r_s)e^{\hat{\alpha}_1 T}c_{1+} + (r_2 - r_s)e^{\hat{\alpha}_2 T}c_{2+} = 0 \end{cases} \tag{2.39}$$

The final expression for the downwelling and upwelling fluxes are so found:

$$\begin{aligned}F_+(\tau) &= \frac{(r_2 - r_s)e^{\hat{\alpha}_2 T}e^{\hat{\alpha}_1 \tau} - (r_1 - r_s)e^{\hat{\alpha}_1 T}e^{\hat{\alpha}_2 \tau}}{(r_2 - r_s)e^{\hat{\alpha}_2 T} - (r_1 - r_s)e^{\hat{\alpha}_1 T}}F_0 \\ F_-(\tau) &= \frac{(r_2 - r_s)r_1 e^{\hat{\alpha}_2 T}e^{\hat{\alpha}_1 \tau} - (r_1 - r_s)r_2 e^{\hat{\alpha}_1 T}e^{\hat{\alpha}_2 \tau}}{(r_2 - r_s)e^{\hat{\alpha}_2 T} - (r_1 - r_s)e^{\hat{\alpha}_1 T}}F_0\end{aligned} \tag{2.40}$$

Now the medium reflectance r, as seen from the top, may be easily calculated:

$$r \equiv \frac{F_-(0)}{F_+(0)} = \frac{(r_2 - r_s)r_1 e^{\hat{\alpha}_2 T} - (r_1 - r_s)r_2 e^{\hat{\alpha}_1 T}}{(r_2 - r_s)e^{\hat{\alpha}_2 T} - (r_1 - r_s)e^{\hat{\alpha}_1 T}} \tag{2.41}$$

or equivalently by introducing the function:

$$f_s \equiv \frac{r_s - r_1}{r_2 - r_s} \tag{2.42}$$

$$r = \frac{r_1 + f_s r_2 e^{(\hat{\alpha}_1 - \hat{\alpha}_2)T}}{1 + f_s e^{(\hat{\alpha}_1 - \hat{\alpha}_2)T}} \tag{2.43}$$

Since $\hat{\alpha}_1 \leq 0$ and $\hat{\alpha}_2 \geq 0$, it is apparent that r_1 represents the top reflectance of an infinitely thick ($T \to +\infty$) medium.

Chapter 3

Instruments

3.1 Introduction

In this chapter all the instruments used in this work for ground-based and satellite measurements will be described. CHRIS sensor on board of PROBA platform provides us the satellite images from which we try to extract vegetation parameters. SPEC-PRO and LAI-2000 give us the possibilities to get ground-based canopy measures, the former to feed our retrieval algorithms, the latter for validating the CHRIS data processing results.

3.2 CHRIS-PROBA

This section is divided into two subsections devoted to descriptions of the PRoject for On-Board Autonomy (PROBA) platform and Compact High Resolution Imaging Spectrometer (CHRIS) sensor.
Mission objectives are principally scientific and technological. First, from a scientific point of view, data from CHRIS instrument give the possibility to obtain information on aerosol, vegetation, land and coastal properties.
Second, it is possible to study the performances and future shrewdness useful in the design of new instruments and small satellite missions with an on-board autonomy systems.

3.2.1 PROBA platform

PROBA's development has been led by the Verhaert consortium supported by ESA. The platform, a computer generated picture of which is shown in figure (3.1.a), was launched on October 22nd 2001 from Sriharikota in southeast Indian coast. It is a small satellite with a new on-board autonomy system, for attitude and orbit control, computer and telemetry. The sattelite payload of platform is composed, apart from CHRIS sensor, by a radiation measurement sensor called SREM, a debris measurement sensor called DEBIE, a wide angle Earth pointing camera, a star tracker and gyroscopes. In figure (3.1.b) is shown the internal structure of the platform. PROBA is 3 axis sta-

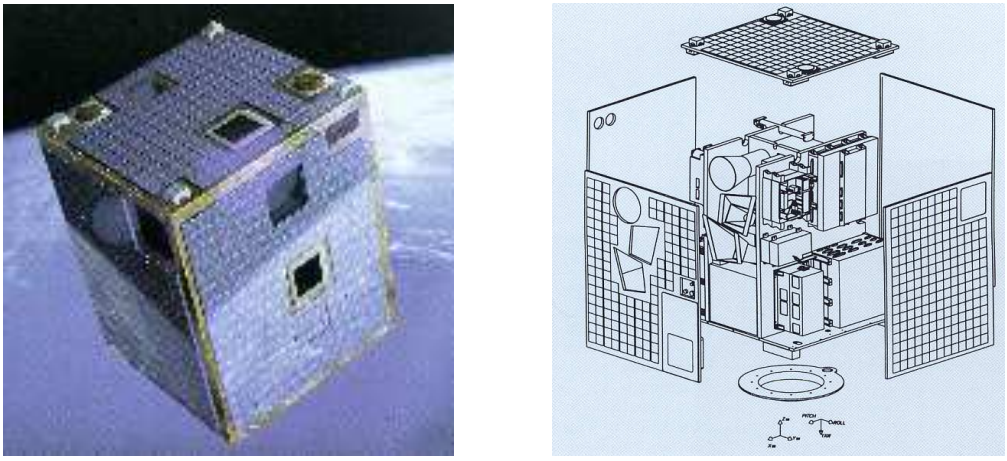

(a) (b)

Figure 3.1: *Figure (a) shows a computer generated picture of PROBA platform. (b) shows a schematic view of the internal structure of the satellite.*

bilized which provides nadir, off-nadir or inertial pointing (information from CHRIS-PROBA official website *http://www-chris-proba.org.uk*). It includes an autonomos double head star tracer, navigation and attitude with GPS sensor, magneto-meters and magneto-torquers, momentum wheels, high per-

formance RISC computer[1], a solid state mass memory of 1.2 Gbits which can be downloaded every 12 hours given ground station visibility and data down-link capacity and an high performances digital signal processor.
PROBA satellite is flying on a Sun-Synchronous orbit at a mean altitude of $615km$. In table (3.1) are reported the main characteristics of PROBA orbit. Moreover in table (3.2) the Attitude Orbital Control System AOCS requirements are listed.

PROBA Orbital Characteristics	
Mean Altitude (range)	615km (560-670)
Type Of Orbit	Sun Synchronous
Equator Crossing Time (descnding node)	10:30 am
Orbital Period	96.94 minutes
Inclination	97.898 degrees
Eccentricity	0.01
Repeat Cycle	approximately 7 days
Orbit Drift	< 2 degrees per year

Table 3.1: *PROBA satellite orbit characteristics.*

PROBA AOCS requirements			
AXIS	Maximum rate for attitude change between imaging periods	Maximum rate excursion during imaging	Range
Pitch	22° in 40 seconds	$\pm 0.3°/s$	$\pm 38°$
Roll	60° in 300 seconds	$0°/s$ (nominal)	$\pm 30°$
Yaw	-	$0°/s$ (nominal)	-

Table 3.2: *PROBA AOCS system characteristics.*

[1]Reduced Instruction Set Computer, a type of microprocessor that recognizes a relatively limited number of instructions but they can execute their instructions very fast

3.2.2 CHRIS instrument

CHRIS instrument was developed by SIRA Electro-Optics Ltd with support from the BNSC. It is a compact hyperspectral and high spatial resolution spectrometer, which dimensions are 200 x 260 x 790 mm, weight is about 15 Kg, that operates in the "push-broom" mode[2]. Figure (3.2) shows CHRIS sensor (figure a) and a schematic view of instrument optics (figure b).

Apar from its fixed field of view of 1.3°, that gives a mean ground swath of

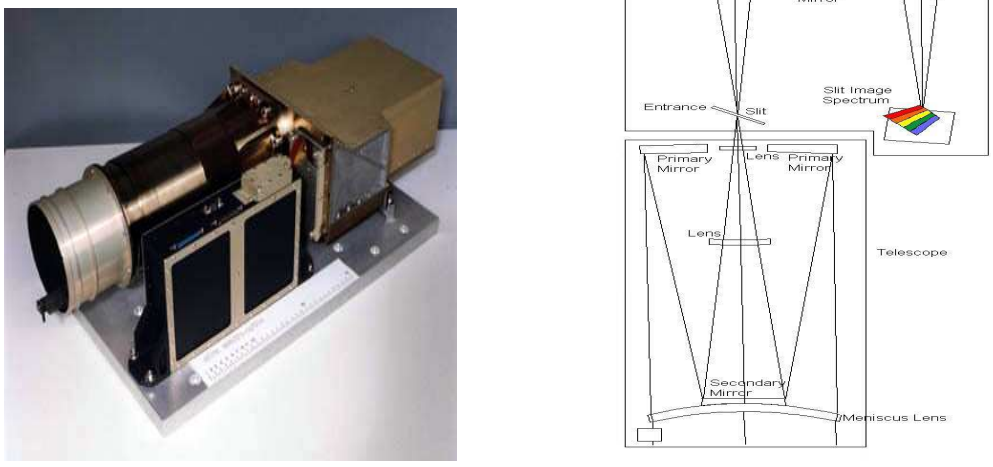

(a) (b)

Figure 3.2: *Figure (a) shows a picture of CHRIS sensor. (b) shows a schematic view of the optics structure.*

14 x 14 km, it is a very versatile sensor. It can acquire spectra over the same ground region in five different viewing geometry sets. These being taken at along track angles of ±55 degrees, ±36 degrees, and nadir.

Ground spatial resolution and spectral bands configuration depend on ac-

[2]The push-broom scanner or linear array sensor is a scanner without any mechanical scanning mirror but with a linear array of solid semiconductive elements which enables it to record one line of an image simultaneously

quisition mode (detailed information are available on CHRIS-PROBA official web site: http://www.chris-proba.org.uk). In any case, CHRIS spectral range goes from 400 to 1050 nm. Main characteristics of CHRIS sensor are summarized in table (3.3).

Each CHRIS image is about 131 Mbits, then, it can store several sets of images, acquired at different viewing angles, in its mass memory of about 1 Gbit. Data are downloaded from SIRA group where the first analysis and calibration are done and, successively, delivered to any users.

CHRIS key characteristics	
Spatial sampling interval	18m on ground at nadir
Image area	14 X 14 km (748 X 748 pixels)
Number of images	Nominal is 5 downloads at different view angles
Data per image (for a 14 X 14 km)	131 Mbits
Spectral range	410 nm to 1050 nm
Number of spectral bands	19 bands at a spatial resolution of 18 m, 63 bands at 36 m
Spectral resolution	from 1.3 nm at 410 nm to 12 nm at 1050 nm (i.e it varies across the spectrum)
Across track pixel size	18 m or 36 m
Digitisation	12 bits
Signal-to-noise ratio	200 at a target albedo of 0.2

Table 3.3: *CHRIS sensor key characteristics.*

3.3 SPEC-PRO

SPEC-PRO is a portable spectroradiometer able to record radiation in the spectral range from 350 nm up to 2500 nm. Wavelength spectral sampling, independent from spectral resolution, is 1.4 nm between 350 and 1000 nm, 2 nm from 1000 nm to 2500 nm. By the way, the resolution is defined as the

Figure 3.3: *Field SPEC-PRO instrument with the endowment computer for a real time data analysis.*

Full Width at Half Maximum of the instrument response to a monochromatic source. SPEC-PRO FWHM is 3 nm in spectral region between 350 and 1000 nm, 10 nm from 1000 nm to 2500 nm. Instrument directly provides as output data radiance, reflectance and transmittance. Normalization operations are made taking a white reference spectra before vegetation measurements, in the same illumination conditions. Instrument is provided with a laptop for a real time in situ data analysis. In table (3.4) are listed the main technical characteristics of SPEC-PRO instrument.

3.4 LAI-2000

LI-COR LAI-2000, shown in figure (3.4), is a plant canopy analyzer used for a rapid and non-destructive leaf area index measurements. Acquisitions can be made above and below the canopy.

The instrument, with a field-of-view of 148° (zenith cutoff angle = 74°), uses fisheye optics to project a canopy hemispheric image onto five silicon detectors. These are concentric circles able to measure light interception at five different zenith angles 7°, 23°, 38°, 53° and 68° (Gower S.T. and Norman

SPEC-PRO main characteristics	
Spectral Range	350 ÷ 2500 nm
Spectral Resolution	3 nm at 700 nm 10 nm at 1400/ 2100 nm
Samping Interval	1.4 nm at 350÷1050 nm 2 nm at 1000÷2500 nm
Scanning Time	100 milliseconds
Detectors	One 512 element Si photodiode array 350÷1000 nm Two separate, TE cooled, graded index InGaAs photodiodes 1000÷2500 nm
Input	Optional foreoptics available
Noise Equivalent Radiance (NeDL)	UV/VNIR 1.4 x 10 -9 W/cm 2 /nm/sr at 700nm NIR 2.4 x 10 -9 W/cm 2 /nm/sr at 1400nm NIR 8.8 x 10 -9 W/cm 2 /nm/sr at 2100nm
Weight	7.2 kg

Table 3.4: *SPEC-PRO sensor key characteristics.*

Figure 3.4: *LI-COR LAI-2000 instrument with the sensor used in LAI measurements.*

J.M, 1991), see figure (3.5.a) and (3.5.b). Moreover, there is a mirror to reflect radiation received by the lens and, finally, a 490 nm filter, which minimizes the contribution of radiation scattered by the foliage.

Our measurements have been taken below pine forest canopy of San Rossore

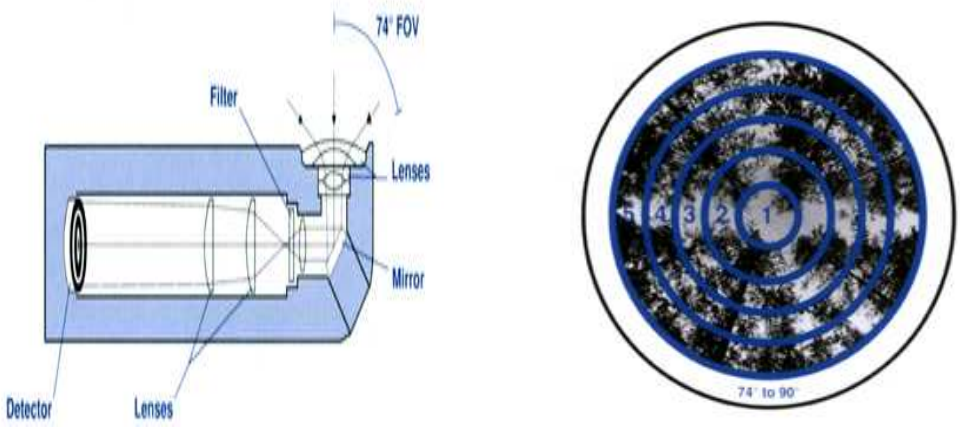

(a) (b)

Figure 3.5: *Figure (a) shows a schematic view of the LAI-2000 optics. (b) shows a schematic view of the five concentric silicon detectors of the instrument.*

Natural Park. Acquisitions are made by positioning optical sensor toward the canopy you have to analyse. As the start button is pushed the instrument gives automatically the Leaf Area Index value. LAI estimation is based on a radiative transfer code in vegetative canopies that assumes:

- Foliage is black: below-canopy measures do not include radiation reflected or transmitted by foliage;
- Single leaf are small compared to the view area of each ring;
- Foliage is randomly distributed within certain foliage containing envelopes;
- Foliage is azimuthally randomly oriented.

Each detector ring views a different portion of canopy (or sky) centered on one of the five viewing angles. Gap Fraction is the fraction of diffuse incident radiation passes through a plant canopy for each viewing angle θ as in equation:

$$T(\theta) = \frac{I_b(\theta)}{I_a(\theta)} \tag{3.1}$$

where $I_b(\theta)$ is the diffuse intensity below the canopy at view angle θ and $I_a(\theta)$ is the diffuse intensity above the canopy at view angle θ.
Defining $S(\theta)$ as the pathlength througth the canopy for each viewing angles we can write the density foliage ρ as:

$$\rho = -2 \int_0^{\pi/2} \frac{\ln(T(\theta))}{S(\theta)} \sin(\theta) d\theta \tag{3.2}$$

For a full cover canopy of high z we have $S(\theta) = z/cos(\theta)$ and $LAI = \rho \cdot z$. Finally equation (3.2) can be rewritten as:

$$LAI = -2 \int_0^{\pi/2} \ln(T(\theta)) \cos(\theta) \sin(\theta) d(\theta) \tag{3.3}$$

LAI-2000 implements equation (3.3) by numerical integration over the 5 viewing angles. As suggested by Gower and Norman (Gower S.T. and Norman J.M, 1991) coniferous have not randomly distributed foliage. To take into account clumping effects LAI measured data have to be corrected by a factor $R = 1.6$.

Chapter 4

Measurements on test site

4.1 The San Rossore Test Site

For this work the San Rossore Natural Park has been chosen as test site. This area, located in Italy, Tuscany region, as shown in figure (4.1.a), is already an official test site of CHRIS-PROBA project and there are many other research teams involved in many experiments (like the European CARBOEUROFLUX, FLUXNET etc.) for the extraction of information on the status and evolution of the park vegetation.

San Rossore is a 24000 hectares flat area along the Tyrrhenian sea-coast line, near the city of Pisa. Its soil is sandy and vulnerable to the infiltration of saline water which can damage vegetation. The Mediterranean climate of San Rossore is charcterized by an average temperature of 15°C and rainfall of about 900 $mm/year$, with a minimun during summer. In figure (4.1.b) we can see a detailed image of the site obtained from CHRIS-PROBA image of September 18th 2003.

Approximatively one third of the park is covered by wood. This portion is mainly domitated by the presence of Mediterranean Pine Forest, maritime pine (Pinus Pinaster) and domestic pine (Pinus Pinea), planted in the XVI century. Maritime pines are present in narrow strips close to the sea-coast line because of their considerable resistance to the strong wind coming from

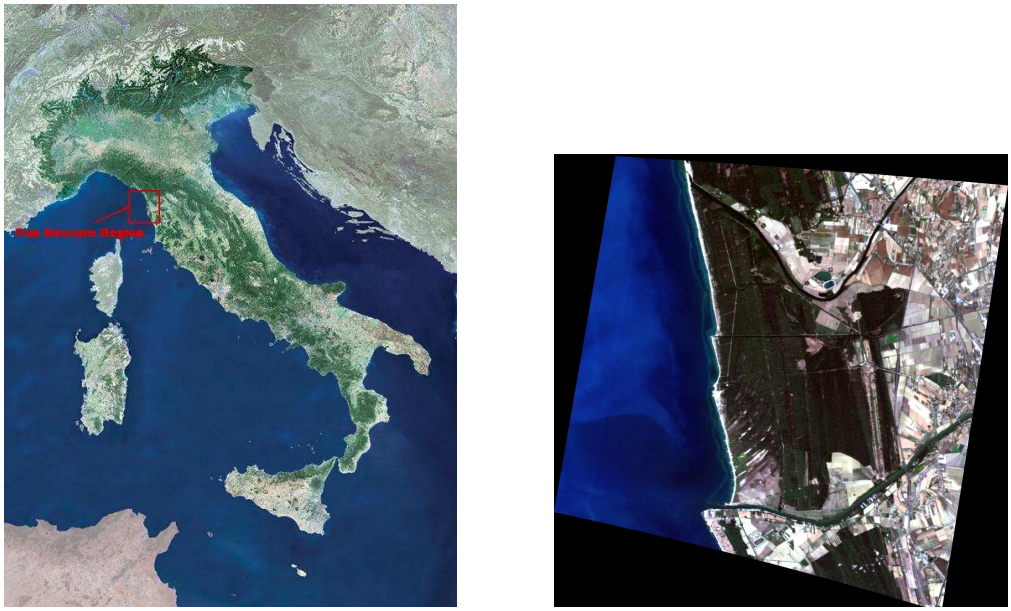

(a) (b)

Figure 4.1: *Figure (a) shows an image of Italy from MERIS (Medium Resolution Imaging Spectrometer) instrument on ESA's Envisat satellite. Red square shows the San Rossore Natural Park Region. Figure (b) is a San Rossore Natural Prak view from CHRIS-PROBA image of 2003 september 18th in the RGB composition from CHRIS spectral channels 8,5,2.*

the sea. Beyond these strips of Pinus Pinaster there are large extentions of domestic pines. Figure (4.2.a) shows the complete San Rossore biomes map. While in figure (4.2.b) we can see only the park covered by maritime and domestic pine.

4.1.1 Maritime Pine

It is an evergreen coniferous tree. We can find Pinus Pinaster near the sea-coast line. These plants can be very tall, up to 35 meters. Its trunk, initially straight, tends to grow slanting, with depth grooves in the bark. The leaves are usually 15-20 cm long and stiff with two needle shaped leaves per fascicle. The cones produced by the maritime pine are 10-20 cm long but they did

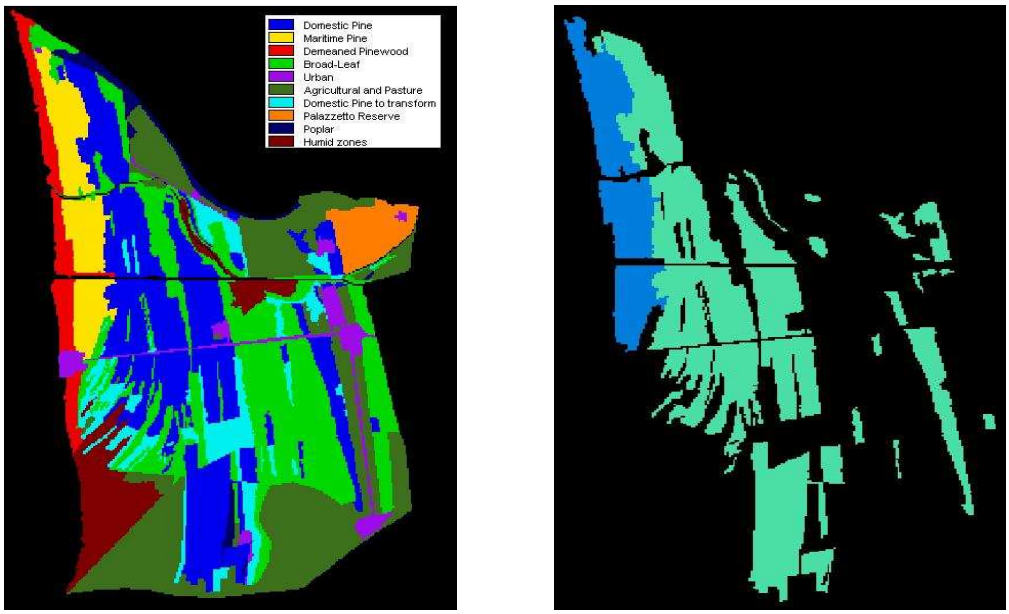

(a) (b)

Figure 4.2: *Figure (a) shows a San Rossore Natural Park Biomes map. In Figure (b) we can see only pixels corresponding to the maritime (dark blue) and domestic pine (blue) biomes.*

not produce the pine kernel.

4.1.2 Domestic Pine

It is an evergreen coniferous tree. We can find Pinus Pinea even very far away from the sea. These plants can be up to 25 meters tall. Their trunks are straight and usually fork into two branches. The leaves are usually 12-15 cm long, stiff and direct principally towards the sky. The cones have a diameter of 10-12 *cm* and they produce a lot of pine kernels.

4.2 LAI and Reflectance measurements

Since the main goal of this work is to retrieve both vegetation and soil parameters from remote sensing observation we need images with spatial resolution

high enough to be sensitive to the gaps between vegetation. As shown by Price in its pioneer work (Price J.C., 1993) this sensitivity becomes insufficient for spatial resolution lower then 100 m.
The primary vegetation parameter we aim at retrieving is the Laef Area Index (LAI) which is defined, for coniferous, as half the total needle surface per unit ground area.
As derived product we attemp to retrieve the fraction of absorbed (by plants) photosynthetically active radiation (FaPAR).

4.2.1 Remote Sensing Reflectance Measurements

CHRIS-PROBA images

Remote sensing measurements come from CHRIS-PROBA acquisitions. Images are composed by pixels with a mean spatial resolution of 20 x 20 meters as a composition of eighteen spectral channels[1]. In this work we take into account only NADIR view acquisitions.
CHRIS-PROBA measures radiation coming from the Earth-Atmosphere system. Photons scattered by the Atmosphere and/or reflected by the Earth surface are counted. Images have been downloaded by SIRA Group, where a first calibration is performed. Successively, values of calibrated radiance, in $W \cdot m^{-2} \cdot sr^{-1} \cdot nm^{-1}$, for each pixel are delivered.

Calibration and Atmospheric correction

When remote sensing images have to be processed in order to retrieve vegetation parameters, such as LAI and FaPAR, or soil reflectance, the original data have to be correct for the atmospheric effects. Calibration and Atmospheric correction algorithm, for CHRIS-PROBA images used in this works,

[1]CHRIS-PROBA spectral channels range from visible ($450nm$) to near infrared ($1050nm$)

has been developed by the IFAC[2] Earth Observation Division (Barducci et al., 2005).

CHRIS data processing starts with a quality assessment analysis consisting in the calculation of some parameters, like Energy E, standard deviation σ, for each image and every spectral band. Results show that Level 1-A data, as provided by SIRA, exibit a low calibration accuracy that produces a coherent noise pattern on the images. For this reason a "de-striping" procedure has been applied to the SIRA data obaining new re-calibrated CHRIS images (Lavel 1-B data).

At a stretch, atmospheric correction algorithm has been developed in order to obtain corrected surface reflectance maps. The adopted model consider molecules (Rayleigh scattering) and aerosol (single and multiple scattering) effects on photons crossing the atmosphere as a purely additive term to the radiance reflected from the target. In the visible and near-infrared range the spectral hemispherical reflectance, $\rho(\lambda, \vartheta)$, is given by equation (4.1):

$$\rho(\lambda, \vartheta) = \frac{\pi[L_{1B}(\lambda, \vartheta) - L_u(\lambda, \vartheta)]}{E_0(\lambda, \zeta)T(\lambda, \vartheta)\cos(\vartheta)} \tag{4.1}$$

where $L_{1B}(\lambda, \vartheta)$ is the spectral radiance reaching the sensor, $L_u(\lambda, \vartheta)$ is the atmospheric path radiance, $E_0(\lambda, \zeta)$ is the TOC total irradiance, $T(\lambda, \vartheta)$ is the atmospheric transmittance from ground to the sensor, ϑ is the angle between the local nadir and the viewing directinon and, finally, ζ is solar zenith angle. Atmospheric radiative transfer computation have been performed by means of MODTRAN 4 (Berk A. et al., 2000) based on DISORT routine (Stamnes K. et al. 1988).

After atmospheric correction CHRIS-PROBA images give us an approximation of the TOC reflectance measured which would be in absence of any atmosphere. This physical quantity corresponds to the r variable in the two

[2]IFAC is the Applied Physics Institute of the Italian National Council of Research (CNR)

streams approximation as seen in equation (2.41) and (2.43).

4.2.2 Measurements on Test Site

As in any retrieval procedure the results have to be validated. Validation was peformed basing on the LAI and soil reflectance ground measurements done in San Rossore. Campaign measurements were carried out at the same time of some satellite passages over San Rossore area: June 16th 2003, May 11th 2004, July 15th 2004, July 29th 2004 and September 8th 2004. Operators positions were located by means of a portable GPS sistem. In this way it has been possible to find the location of the all the validation points into the CHRIS-PROBA georefered images.

LAI measurements

Canopy LAI has been measured by means of LI-COR LAI-2000 instrument (LAI-2000 User's Guide, 2005; Gower S.T. and Norman J.M., 1991; Chen J.M., et al., 1997).
Radiation attenuation under the canopy is caused not only from needles but even from trunk and branches. This means that what we are really measure with LAI-2000 is the ***Plant Area Index*** and not the ***Green Leaf Area Index***, that is what we expect to retrieve from remote sensing observation. Table (4.1) summarizes canopy LAI values measured in San Rossore Natural Park. Positions are given by the X,Y Gauss-Boaga coordinates.

Soil reflectance spectra

In addition to those taken in the same position of LAI ground measurements, soil reflectance spectra have been measured also in some other points, even out of the pine forest, on green, sandy, dry and wet soil.
Measurements have been performed by means of FieldSpec-Pro Spectro-radiometers (Hatchell D.C., 1999) which acquires reflectance spectra from

03-06-16 measured LAI			
ID	X	Y	LAI
2	603634	4844498	4.2
3	603581	4843751	4.3
4	603537	4842670	4.5
5	603272	4842303	3.7
6	604763	4841699	4.8
7	604755	4840383	4.2
8	604355	4843257	4.6
9	604173	4844388	4.2
10	603989	4844896	5.1
04-09-08 measured LAI			
2	603634	4844498	3.7
3	603581	4843751	4.0
5	603272	4842303	3.8
7	604755	4840383	4.5
8	604355	4843257	3.9

Table 4.1: *Values of ground based LAI measurements carried out in San Rossore Natural Prak on June 16th 2003 and September 8th 2004 in points identified by X-Y coordinates taken by means of GPS portable instruments.*

$350nm$ to $1200nm$. For each selected points five acquisitions have been taken, corresponding to five different viewing geometry: the first at nadir viewing, then, at a viewing zenith angle of 45°, at four different azimuth angles: 45°, 135°, 225° and 315°. In this way, the integration of the five measures give us a good approximation for the upward hemispherical reflectance of the target. Finally, the solar zenith angle was more or less the same than the one of the CHRIS-PROBA acquisition.

Measurements of soil spectra will be used to validated the soil line extraction by satellite images. Spectra shown in figure (4.3) have been obtained from nadir viewing geometry in some representative selected Park's points. As said we have chosen zone with sandy soil, undergrowth, dry soil and wet soil and finally soil with neddles. All these measures have been acquired

on July 15th 2004. From spectra shown in figure (4.3) we have selected all

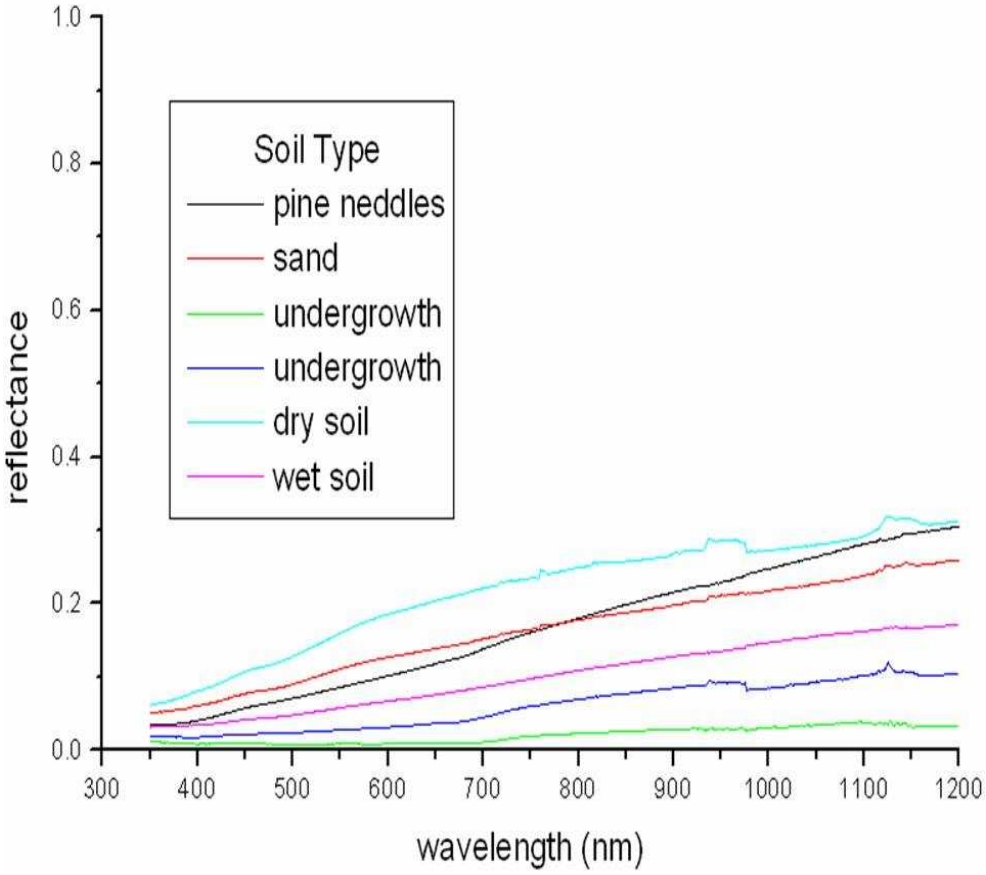

Figure 4.3: *Soil reflectance spectra measured on San Rossore, on July 15th 2004. We have considered only nadir viewing geometry in some ad-hoc selected points: Undergrowth soil, soil with neddles, sand, dry soil and wet soil.*

the reflectances values corresponding to the RED and NIR CHRIS-PROBA channels (the same used in the retrieval processes described in chapter 5). The mean of RED and NIR values should identify a soil line of the Park that should be "equal" to the soil line extracted from CHRIS-PROBA images. Ground-based soil line is shown in figure (4.4) where we can see that constant parameters are $a = 1.26$ and $b = 0.04$.

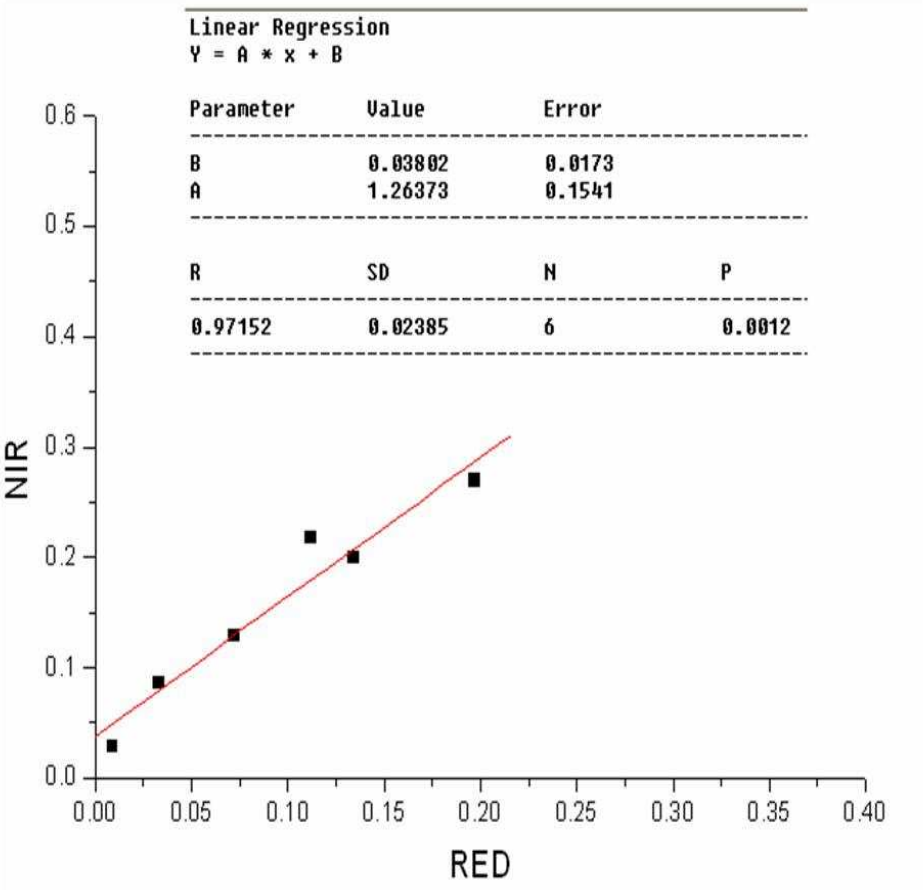

Figure 4.4: *Soil line extracted from reflectance spectra measured on San Rossore, on July 15th 2004 (show in figure 4.3). We have indicated even the results of the linear fit used to extract the line where we can note a very good* $R = 0.97152$ *coefficient.*

4.2.3 LAI and Reflecance measurements in Florence Laboratory

As said in section (2.4) the knowledge of the extinction coefficient α and of the infinitely thick canopy reflectance r_∞ is needed for solving the LAI problem. This task can be attempted by means of laboratory measurements. First of all we took from San Rossore trees some little branches of maritime and domestic pine. In Florence we built up a cubic box of 1 meter side, with an hole, of $20cm$ in diameter, in the upper face. All the internal faces were

painted black in order to obtain an approximation of *black body*.

On the top of the box two alluminium hemi-circles, of about 1.4 meters di-

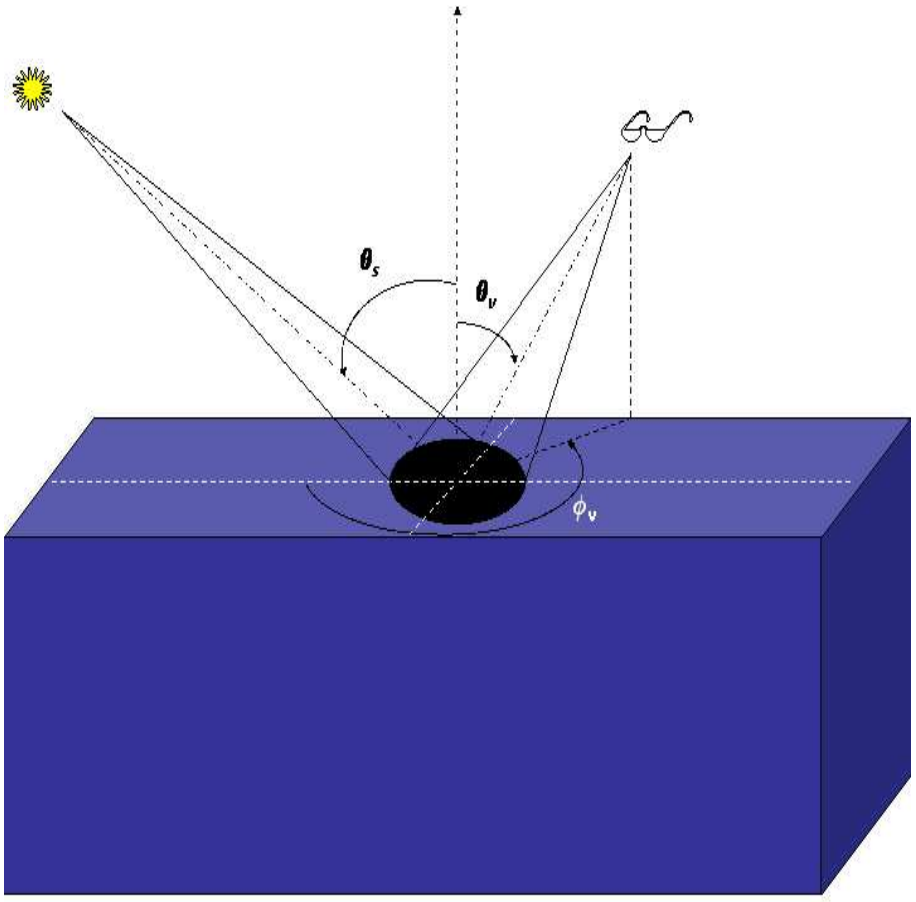

Figure 4.5: *Schematic view of geometry of laboratory measurements of canopy reflectance. We have considered a constant (in one hour of observation between noon and 1:00 pm) solar zenith angle, solar azinuth angle* 0° *viewing zenith angle of* 45° *and viewing azimuth angle of* 45°, 135°, 225° *and* 315°.

ameter, to create a hemi-sphere circumscribing the upper face, were mounted. The hemi-circles cross point was coincident to the hole center. In this way, placing the spectroradiometer's sensor in downward direction at the cross point we perform a nadir reflectance measurements, while, placing it at half way the cross and the four basis points measurements at a viewing angle of

45° and azimuth of 45°, 135°, 225° and 315° are performed[3]. The integra-

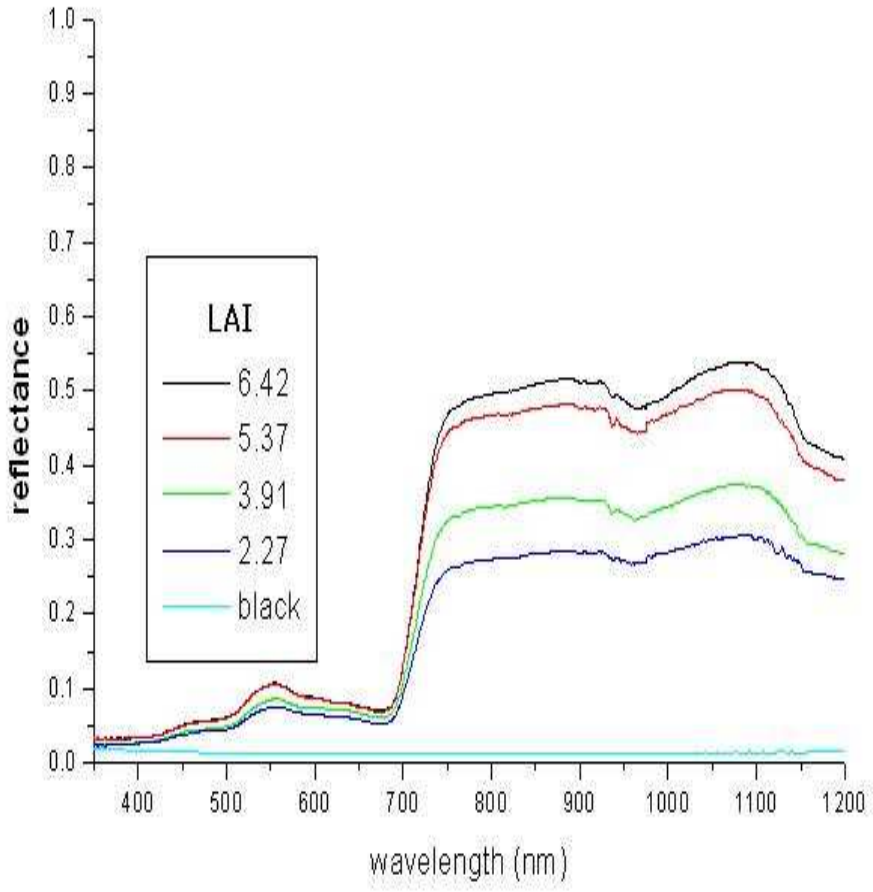

Figure 4.6: *Reflectances spectra for different LAI values measured on Florence Laboratory on a maritime pine branch. Black line correspond to the black body spectrum.*

tion of all these reflectances provides a good approximation for the upward hemispherical reflectance of the target. A schematic representation is shown in figure (4.5).

The little pine branches were about $30cm$ tall and $20cm$ large (like the black hole). They were fixed between the hemi-circles cross point and the hole center. For each branch four sets of measures, corresponding to four LAI

[3]Note that viewing geometry are the same of San Rossore measures described in the previous section

values, were performed. Every set was composed of six acquisitions: five at the different viewing geometry described above and one corresponding to the black body. Different values of LAI was obtained to remove some needles from the branch. Measurements were made always pointing the sensor to the center of the hole. As obvious the acquired reflectance values depend on the amount of needels: small LAI (small needle amount give small LAI) implies that the radiation can more easily reach the black background where it is absorbed. While for large LAI many scattering processes occur and photons can more easily be backscattered to the sensor. It is apparent that large LAI produces higher reflectance than small LAI. An example of reflectance spectra, for different values of maritime pine LAI, is shown in figure (4.6). As visible the measured reflectance follows the increasing trend with LAI.
After the reflectance acquisitions we have measured the lenght l of every single needle-couple by the callipers, assuming that the couples can be approximated as a cylinder. For a randomly chosen subset of 25 couples we have also measured their diameter d to extract a linear relation between lenght and diameter $d = a + bl$. Finally branches LAI have been calculated with the formula (4.2):

$$LAI = \frac{\frac{1}{2} \cdot \sum_{needles} \left(1 + \frac{\pi}{2}\right) \cdot l \cdot (a + bl)}{\pi r_{bh}^2} \tag{4.2}$$

where r_{bh} is the black hole radius. Many physical algorithms, such as the NADIM (Gobron N., et al., 1997) or the KUUSK models (Kuusk, A. and Nilson T., 2000), need the features of the single leaf and its optical properties (like radius, reflectance, etc.) to simulate vegetation response to the solar irradiation. Usually the single leaf shape is assumed flat and circular but in case of conifers it is hard to approximate neddles with such a shape. In this work we consider as "single leaf" the little branch described above. In this way, with LAI values and reflectance spectra coming from laboratory

measurements we are able to compute the physcal parameters (for instance extinction coefficient, infinity canopy reflectance etc.) needed in the canopy LAI inversion model, as described in chapter 5.

Chapter 5

Data Processing Algorithms

5.1 Introduction

In this chapter we will describe methods and algorithms developed to compute vegetation canopy parameters from satellite (CHRIS-PROBA) and ground based (LI-COR and SPEC-PRO) measurements.
The use of high spatial resolution data (as CHRIS-PROBA images of $20\times20m$ ground pixels) involves the manipolation of large dimension images. Then the idea for implementing our algorithms consisted of using mathematical formulas as simple as possible, in order to reduce computing time but without taking into account synthetically generated LUTs as done in many other algorithms (Wang Y. et al., 2004; Knyazikhin Y. et al., 1998; Price J.C., 1993).
In the next sections we will describe the approach followed to determine soil line, vegetation scattering coefficients and reflectance of infinity thick canopy. By means of these parameters we have implemented algorithms in order to retrieve LAI, FaPAR and soil reflectance: figure (5.1) shows the whole retrieval flow diagram, from ground based and laboratory vegetation parameters measures up to the satellite image analysis.
Finally, we remark that all the vegetation parameters used in these algorithms have been calibrated over the Pine forest of the San Rossore Natural

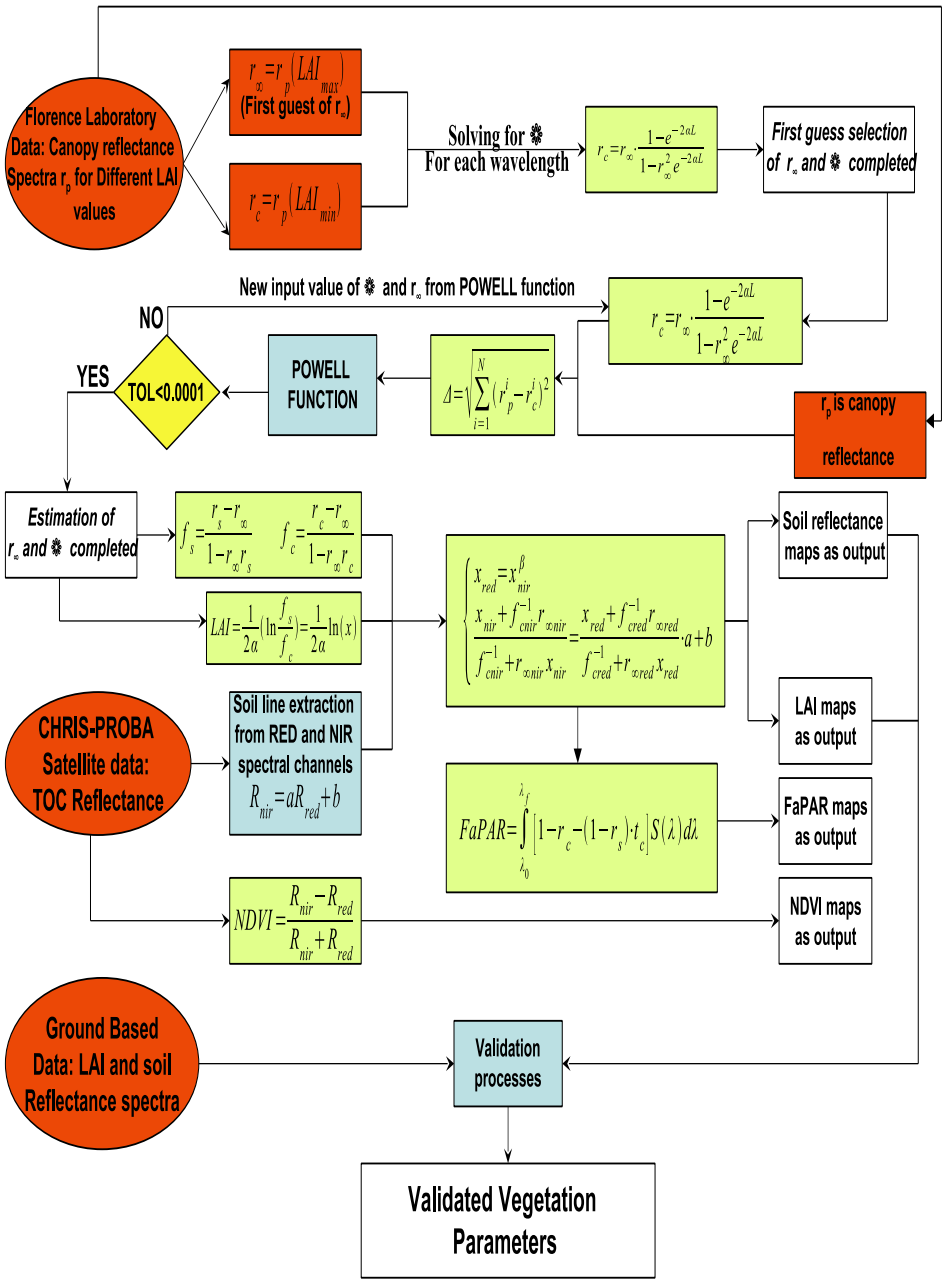

Figure 5.1: *Flow diagram of algorithms developed in our work: from Ground based and Florence laboratory to CHRIS-PROBA image analysis and validation processes.*

Park. Application of this method to other sites or different canopies requires a new calibration and laboratory measures on specific canopy samples.

5.2 Soil line extraction

As described in chapter 2 the two fluxes approximation with symmetric scattering leads to the equation:

$$r_{toc} = \frac{\sigma(\sigma + \gamma \cdot r_s) + \gamma(\gamma - \sigma \cdot r_s) \cdot e^{-2\alpha L}}{\gamma(\gamma - \sigma \cdot r_s) - \sigma(\sigma + \gamma \cdot r_s) \cdot e^{-2\alpha L}} \tag{5.1}$$

with $\alpha = \sqrt{k^2 - \sigma^2}$ and $\gamma = k + \alpha$, where:

r_{toc} is the top of canopy reflectance,

σ is the scattering coefficient,

k is the absorption coefficient.

When we know r_{toc} for $L \to \infty$ and α for each wavelength we have a sistem of M equations with $M + 1$ unknowns to solve which we need an additional equation: we take the **soil line equation** (Price J.C., 1993).

For a given soil type, in this case the San Rossore Natural Park area, there exists an almost linear relation between its RED ($\lambda_1 \cong 630nm$) and NIR ($\lambda_2 \cong 870nm$)[1] reflectance, the so called "soil line":

$$r_{s2} = a \cdot r_{rs1} + b \tag{5.2}$$

where r_{s1} is the RED reflectance, r_{s2} is the NIR reflectance, a and b are constants. Once a and b are known equation (5.2) can be used as $(M+1)th$ equation in soil reflectance and LAI retrieval problem (Benedetti R. et al., 2005). Soil line extraction from spectral maps is possible when we make use of high spatial resolution images. Particularly, in order to have a well defined soil line, a less than $100m$ spatial resolution is recommended (Price, J.C., 1993). CHRIS-PROBA surface reflectance maps (Barducci A. et al., 2002),

[1] For CHRIS-PROBA images used in this work $630nm$ correspond to channel 6 and $870nm$ correspond to channel 15

with a $20m$ mean ground resolution, allow to extract soil line parameters considering RED ($630nm$) and NIR ($900nm$) spectral channels.

From a theoretical point of view the soil line should represent a given soil type in all its possibile conditions so that the merging of different days, months and, why not, years is in principle the best choice. In particular adding reflectance images acquired on different days (and hence soil conditions) a refinement and a better definition of the soil line is expected. As obvious this is true only if sensor calibration and atmospherical correction do not introduce different bias and distortion on the reflectance data used.

Just to check the reliability and mutual coherence of the images we have generated scatter plots of NIR versus RED reflectance for each single images and for all the images together.

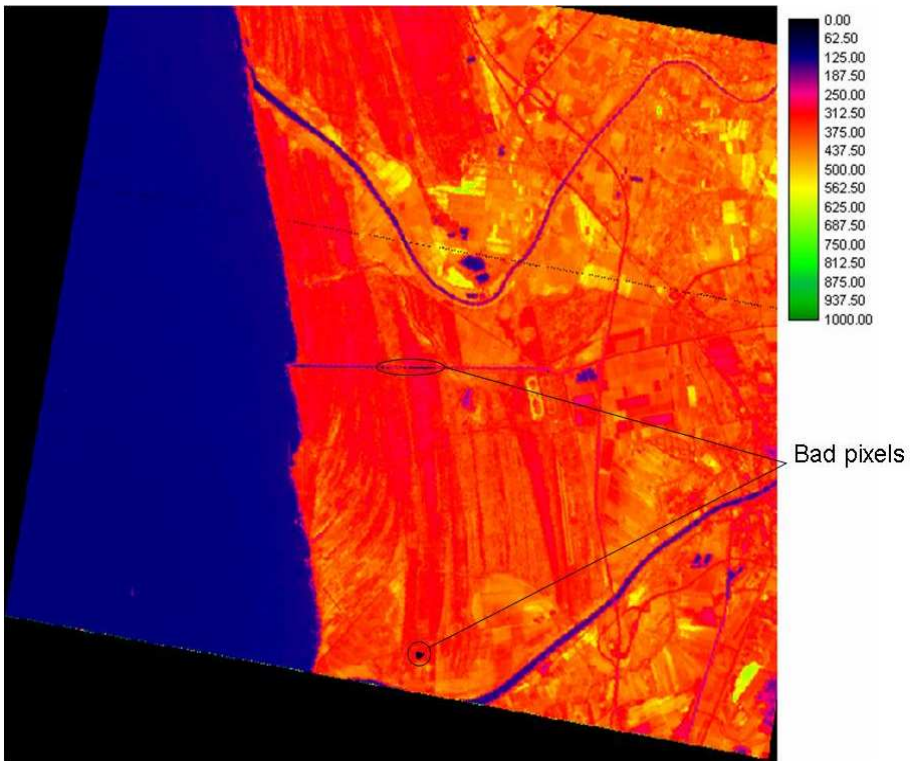

Figure 5.2: *July 25th 2003 CHRIS-PROBA Channel 15 map. Bad pixels are signed as black pixel.*

5.2.1 Soil line on single CHRIS-PROBA images

We take, for example, the CHRIS-PROBA maps acquired on July 25th 2003. Channel 6 (631.0nm) and 15 (870.3nm) give us the scatter plot shows in figure (5.3.a). It is clear that there are some bad pixels. These may be due to an error in the CHRIS-PROBA image georeferentation process or in a bad classification of some pixels in the reference vegetation map (Figure 4.2.a).

Nevertheless, bad pixels are 582 on 70000 pine forest pixels, a very little

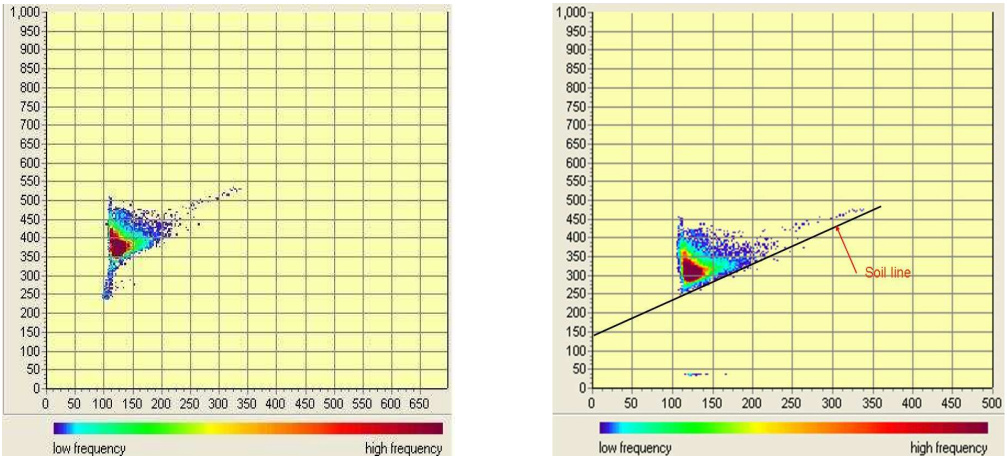

(a) (b)

Figure 5.3: *Figure (a) show the Scatter plot of July 25th 2003 CHRIS-PROBA map. On X axis we have the RED reflectance (630 nm) on the Y axis the NIR reflectance (870 nm). Bad pixels have RED reflectance < 125 and NIR reflectance < 250. Plot (b) show the correct scatter plot of July 25th 2003 CHRIS-PROBA maps without bad pixels where the soil line has been traced.*

percentage, about the 0.8%. Moreover, because of their well defined localization, as shown in figure (5.2), it is resonably supposed that in our analysis, and then in the soil line evaluation, these pixels can be rejected. After this correction we obtain a new well defined scatter plot as shown in figure (5.3.b). The same procedure has been applied to all CHRIS-PROBA images obtaining the scatter plots, with their relative soil lines, shown in figure (5.4). Scatter plot (a) is for June 16th 2003 with line parameters $a = 0.9$ and $b = 0.15$,

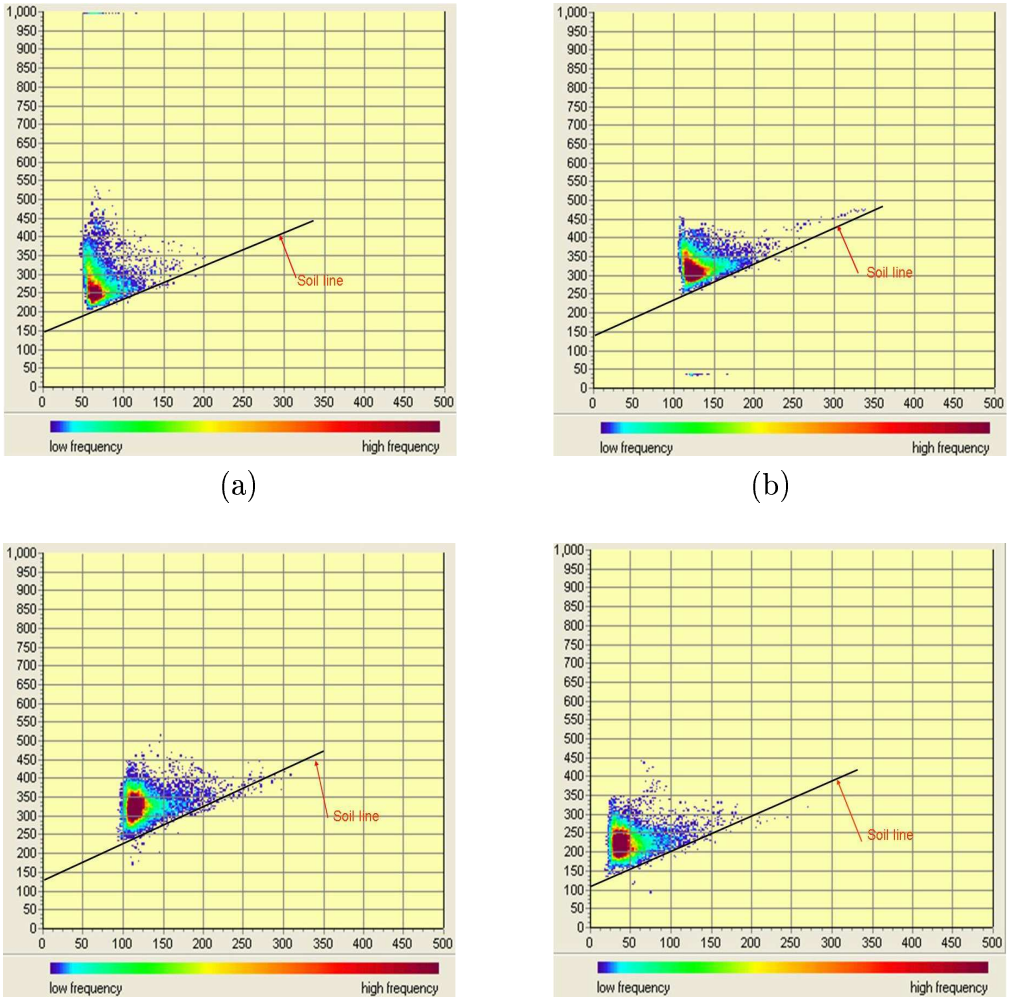

Figure 5.4: *Scatter plot for the four CHRIS-PROBA images analized in our work over the San Rossore Natural Park. (a) June* 16*th 2003, (b) July* 25*th 2003, (c) September* 18*th 2003, (d) September* 8*th 2004.*

(b) is for July $25th$ 2003 with $a = 1.0$ and $b = 0.13$, (c) is for September $18th$ 2003 with $a = 1.0$ and $b = 0.125$ and (d) is for September $8th$ 2004 with $a = 0.93$ and $b = 0.11$. The best accordance is between images of July 25 and September 18 which give the same value for a and a relative difference of 4% for b coefficient. In table (5.1) are summarized the line constant extracted from CHRIS images.

Image	a	b
june 16 2003	0.9	0.15
july 25 2003	1.0	0.13
september 18 2003	1.0	0.125
september 8 2004	0.93	0.11

Table 5.1: *Constant parameters for soil line obtained from CHRIS-PROBA RED and NIR images*

5.2.2 Unique soil line for all the CHRIS-PROBA images

As previously said if all the used images are comparable in term of calibration and atmospherical correction a better defined soil line is expected. By merging all the single scatter plots we generate the combined scatter plot shown in figure (5.5). Even if the single soil line shown in figure (5.4) are better defined, also the soil line of the merged images (figure 5.5) can be easily traced. Constant parameter are $a = 1.15$ and $b = 0.095$.

In table (5.2) are summarized all the soil line coefficients obtained from NIR versus RED CHRIS data scatter plots and from San Rossore ground-based measurements.

Single (particularly on July 25th 2003 and September 8th 2003) and combined soil line have the angular coefficients a comparable with that of the ground based soil line. On the contrary, b constants are very different. These disagreements could be due to an offset in the NIR CHRIS images that increase the NIR reflectance. This imply a lift of NIR-RED scatter plots whose soil lines are characterized by a greater value of the intercept b. In Appendix B is shown the extraction process of soil line using NIR CHRIS spectral channel 17 (centerd at 907.7 nm) where the reflectance offset is even more visible and combined soil line can not be traced at all.

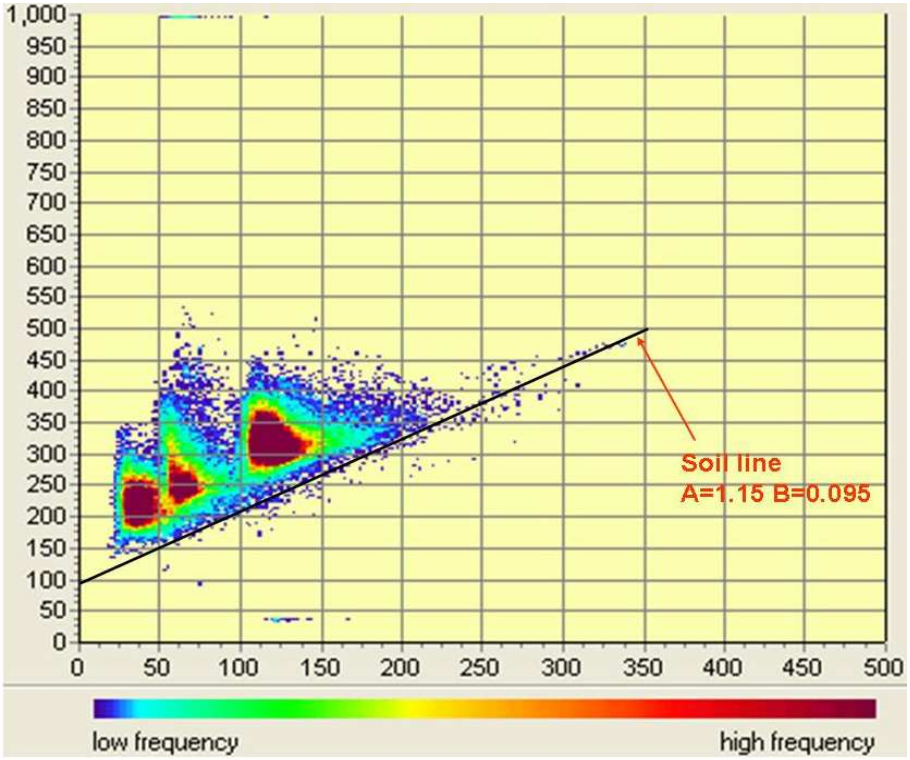

Figure 5.5: *Combined scatter plot of all analized CHRIS-PROBA maps with its soil line. Constant parameter are* $a = 1.15$ *and* $b = 0.095$

Image	slope (a)	intercept (b)
June 16 2003	0.9	0.15
July 25 2003	1.0	0.13
September 18 2003	1.0	0.125
September 8 2004	0.93	0.11
July & Septermber 2003	1.15	0.095
ground based	1.2	0.04

Table 5.2: *Constant parameters for soil line obtained from CHRIS-PROBA NIR vs RED scatter plots and from San Rossore ground based soil reflectance measurements*

5.3 Scattering coefficients and infinity canopy reflectance evaluation

Once we have extracted the soil line parameters, we must evaluate scattering coefficients and infinitely thick canopy reflectance, as required by the two

fluxes approximation of the radiative transfer problem.
The algorithm developed for this analysis is composed of two different sections:

1. first guess of unknown parameters;

2. optimization procedure;

5.3.1 First guess of scattering coefficients and infinity canopy reflectance

First of all we have selected, as our infinitely thick canopy reflectance first guess, the spectra of the pine branch with the largest LAI[2], as measured on Florence Laboratory and described in section (4.2).
From equation (2.43) we can derive that on black soil[3], i.e. $r_s = 0$, the canopy reflectance is given by the expression:

$$r_c = r_\infty \cdot \frac{1 - e^{-2\alpha L}}{1 - r_\infty^2 e^{-2\alpha L}} \tag{5.3}$$

where L is the leaf area index, α is the scattering coefficient, r_∞ is the infinitely thick canopy reflectance. Introducing in equation (5.3) the canopy reflectance r_c of the pine branch with the smallest LAI value and solving it for α we obtain the first guess for the scattering coefficient.

5.3.2 Optimization procedure: final scattering coefficients and infinity canopy reflectance estimation

Once we have obtained first guess for scattering coefficients and infinity canopy reflectance we are able to exctract the final best values.

[2] r_∞ first guess is the black line spectrum (LAI=6.42) shown in figure (4.6)
[3] we are, for istance, in this situation when we have infinity canopy and then we can't see soil effects or, as in our laboratory case, when we measure reflectance on a black hole.

Best-fit procedures is based on POWELL IDL routine applied on the expression (5.3). Powell routine consists in the minimization of the cost function:

$$\Delta = \sqrt{\sum_{i=1}^{N} (r_p^i - r_c^i)^2} \tag{5.4}$$

where N is still the number of measured LAI, r_p^i is the pine branch reflectance measured in Florence Laboratory and r_c^i is the pine branch reflectance computed from the algorithm.

The two fitting parameters are, as obvious, the searched infinite canopy reflectance r_∞ and the scattering coefficient α for every wavelenghts. At the

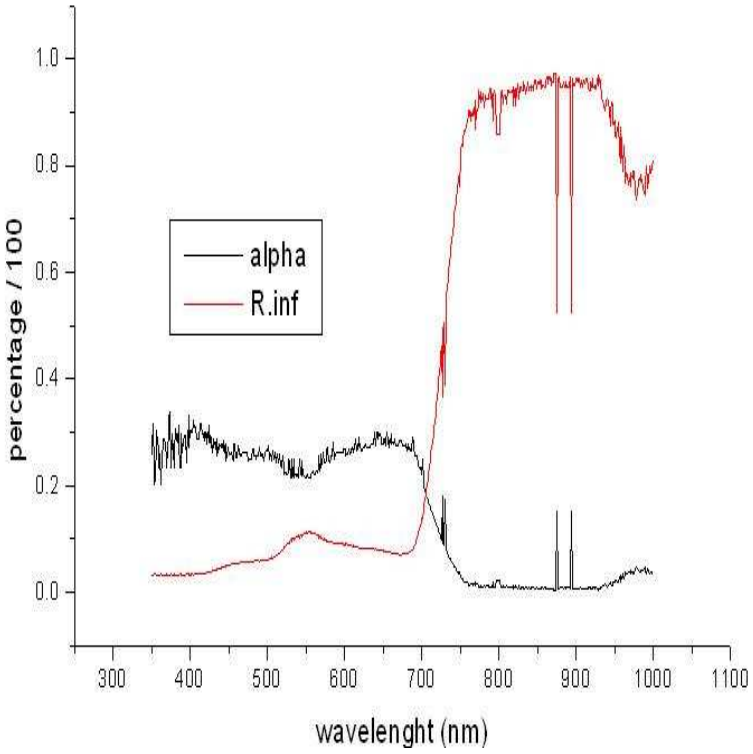

Figure 5.6: *Example of α and r_∞ spectra by May 11th 2004 Florence Laboratory measure.*

end of the minimization procedure we obtain a full spectrum from $350nm$ to $1000nm$ both for r_∞ and α, as shown in figure (5.6).

5.4 Retrieval algorithm for NDVI, LAI, FAPAR and soil reflectance

Considering a symmetric scattering that implies $\alpha_2 = -\alpha_1 \equiv \alpha$, we can rewrite equation (2.43) as:

$$r_c = \frac{r_\infty + \left(\frac{r_s - r_\infty}{1 - r_\infty r_s}\right) \cdot e^{-2\alpha L}}{1 + \left(\frac{r_s - r_\infty}{1 - r_\infty r_s}\right) \cdot r_\infty \cdot e^{-2\alpha L}} \equiv \frac{r_\infty + f_s e^{-2\alpha L}}{1 + f_s r_\infty e^{-2\alpha L}} \tag{5.5}$$

where we have defined for convenience f_s as:

$$f_s = \frac{r_s - r_\infty}{1 - r_\infty r_s} \tag{5.6}$$

In the same way, defining function f_c as:

$$f_c = \frac{r_c - r_\infty}{1 - r_\infty r_c} \tag{5.7}$$

and solving equation (5.5) for L we found that:

$$L = \frac{1}{2\alpha}(\ln f_s - \ln f_c) = \frac{1}{2\alpha} \ln x \tag{5.8}$$

Notice that both f_c and f_s range from -1 up to +1 but, r_c is always lower than r_∞ for $r_s < r_\infty$ and vice versa, and then their ratio x in equation (5.8) is always positive, making in any case the logarithm in the same equation well defined.

5.4.1 NDVI retrieval

Normalized Difference Vegetation Index (NDVI) is an ad hoc parameter with no explicit physical relationship with other vegetation parameters coming from direct and indirect measures or from radiative transfer calculations.
It is a quite robust index able to reveal the amount of vegetated biomass present in image pixels by means of NIR and RED (R_{red}, R_{nir}) measured

reflectance difference. The basis for NDVI is the abrupt increase of vegetation reflectance at the wavelength $\lambda = \lambda_0 \simeq 0.7\mu m$ (Price J.C. and Bausch W.C., 1995): in practice it is the contrast between soil and vegetation in the RED and NIR domains. We can write the NDVI expression as:

$$NDVI = \Delta \ln[R(\lambda_0)] = \frac{R(\lambda_0 + \delta\lambda) - R(\lambda_0 - \delta\lambda)}{R(\lambda_0 + \delta\lambda) + R(\lambda_0 - \delta\lambda)} \equiv \frac{R_{nir} - R_{red}}{R_{nir} + R_{red}} \quad (5.9)$$

where $\delta\lambda$ is of the order of $0.1 - 0.2\mu m$.

In our case R_{red} and R_{nir} are obtained by remote measurements from CHRIS-PROBA. In particular, for R_{red} we use the spectral channel centered at 630 nm and for R_{nir} spectral channel centered at 870 nm.

Results and discussions are shown in the next chapter.

5.4.2 LAI and soil reflectance retrieval

Leaf Area Index (LAI) is one of the most important vegetation parameters and it plays a critical role for understanding many ecophysiological plant processes, such as evapotranspiration and photosyntesis.

It has effects on the radiation exange with the atmosphere throught its effects on albedo and is very important in climate and large-scale ecosystem models (Price, J.C. and Bausch W.C., 1995; Chen J.M., et al., 1997, Mynemi et al., 2002; Wang Y., et al., 2004).

For conifers it can be defined as the hemisurface neddle leaf surface per unit ground area. On the other hand, for broadleaf canopies, it is more obviously defined as one-side green leaf area per unit ground area.

Since LAI is a structural and wavelength independent vegetation parameter we can rewrite equation (5.8) for two different wavelength, λ_1 and λ_2, and equate the right hand terms of 5.8 (which correspond to LAI) so that:

$$\frac{1}{2\alpha_1} \ln\left(\frac{f_{s1}}{f_{c1}}\right) = \frac{1}{2\alpha_2} \ln\left(\frac{f_{s2}}{f_{c2}}\right) \equiv \frac{1}{2\alpha_1} \ln x_1 = \frac{1}{2\alpha_2} \ln x_2 \quad (5.10)$$

Notice that $\alpha_i \equiv \alpha(\lambda_i)$ is the scattering coefficient for wavelength λ_i and analogously for the other variables.

From equation (5.10) we obtain, defining $\beta = \alpha_1/\alpha_2$:

$$x_1 = x_2^{\beta} \tag{5.11}$$

Solving equation (5.6) for r_s, for a generic wavelength i, we obtain that:

$$r_{si} = \frac{f_{si} + r_{\infty i}}{1 + r_{\infty i} f_{si}} \tag{5.12}$$

Considering equation (5.11) and substituting equation (5.12), for wavelength 1 and 2, into soil line equation (5.2) we can rewrite it in terms of f_{ci} parameters and unknowns x_1 and x_2, to get the system:

$$\begin{cases} x_1 = x_2^{\beta} \\ \\ \dfrac{x_2 + f_{c2}^{-1} r_{\infty 2}}{f_{c2}^{-1} + r_{\infty 2} x_2} = \dfrac{x_1 + f_{c1}^{-1} r_{\infty 1}}{f_{c1}^{-1} + r_{\infty 1} x_1} \cdot a + b \end{cases} \tag{5.13}$$

After some simple algebric manipolations we can find the equation to be solved, in general with numerical methods:

$$\begin{aligned} (a r_{\infty 2} + b r_{\infty 1} r_{\infty 2} - r_{\infty 1}) \cdot x_2^{\beta+1} + \frac{a + b r_{\infty 1} - r_{\infty 1} r_{\infty 2}}{f_{c2}} \cdot x_2^{\beta} + \\ + \frac{a r_{\infty 1} r_{\infty 2} + b r_{\infty 2} - 1}{f_{c1}} \cdot x_2 + \frac{a r_{\infty 1} + b - r_{\infty 2}}{f_{c1} f_{c2}} = 0 \end{aligned} \tag{5.14}$$

The root of equation (5.14) gives us the x_2 value. Introducing it into equation (5.8) we can calculate the retrieved LAI values. On the other hand, substituting x_2 into the first equation of the system (5.13) we obtain the x_1 value.

Once we have LAI, we can estimate the function f_{si}, for each spectral channel, by means of simple relation $f_{si} = f_{ci} x_i = f_{ci} e^{2\alpha L}$, and then, using equation (5.12), we are able to evaluate the soil reflectance for each wavelength.

Algorithm described in this section, with the parameters α and r_∞ computed as shown in the previous section, has been implemented in IDL code whose results and their discussions will be shown in the next chapter.

5.4.3 FaPAR retrieval

The Fraction of absorbed (by vegetation) Photosynthetically Active Radiation (FaPAR) is related to the canopy structure and its energy absorption capacity. Then it is another key parameter in order to understand the state and the evolution of canopy. It is useful in most ecosystem productivity models and in global climate, hydrology, biogeochemestry and ecology models (Knyazikhin Y., et al. 1998).

FaPAR in two streams approximation (Benedetti et al., 2005) is defined as:

$$FaPAR = \frac{\int_{\lambda_0}^{\lambda_f} [F_-(0,\lambda) - F_+(0,\lambda) - (1-r_s)\cdot F_-(L,\lambda)]d\lambda}{\int_{\lambda_0}^{\lambda_f} F_-(0,\lambda)d\lambda} \tag{5.15}$$

where λ_0 and λ_f mark the lower and the upper wavelength limits, usually $\lambda_0 = 400nm$ and $\lambda_f = 700nm$. Taking for convenience the mean solar spectrum, $S(\lambda)$, normalized over the spectral band (λ_0, λ_f):

$$\int_{\lambda_0}^{\lambda_f} S(\lambda)d\lambda = 1 \tag{5.16}$$

and assuming that the TOC incident radiation $F_-(0,\lambda)$ is proportional to the mean solar spectrum we can rewrite equation (5.15) as:

$$FaPAR = \int_{\lambda_0}^{\lambda_f} [1 - r_c - (1-r_s)\cdot t_c]S(\lambda)d\lambda \tag{5.17}$$

where r_c is the canopy reflectance, r_s is the soil reflectance and the vegetation canopy transmittance t_c, defined as:

$$t_c \equiv \frac{F_-(L)}{F_-(0)} = \frac{(1-r_\infty)\cdot e^{-\alpha L}}{1 - r_\infty + (r_s - r_\infty)\cdot r_\infty \cdot e^{-2\alpha L}} \tag{5.18}$$

has been introduced.

In FaPAR retrieval process, as we can see from equation (5.17), it is important the sensor hyperspectral capability. Many instruments, at hight spatial

resolution, have only a few spectral band in the range of interest of FaPAR estimation. When we speak of high spatial resolution we are thinking at ground pixels of maximum dimensions of $50 \times 50m$ (Price J.C., 1993).

Chapter 6

Data Analysis

6.1 Introduction

In this chapter we will show the results obtained from CHRIS-PROBA reflectance data. In section 6.2 NDVI maps as obtained applying equation (5.9) directly to RED and NIR CHRIS images are summarized. In addition, results of an NDVI maps statistical analysis are explained as well as the following NIR CHRIS data examination. In section 6.3 are presented LAI and validation processes results. Section 6.4 is devoted to show retrieved pine forest soil reflectances. Section 6.5 shows FaPAR results given by retrieved LAI and soil reflectances. Finally conclusion on the developed algorithms and their results, are presented in section 6.6.

6.2 NDVI results

As we have shown in section (5.4) NDVI is defined by equation (5.9). Even though it is an *ad hoc* vegetation parameter its values can be used for testing the reliability of the LAI/FaPAR retrieval algorithms. Actually, a near-linear relationship between FaPAR and NDVI (Mynemi R.B. and Williams D.L., 1994) and a logarithmic-like distribution between LAI and NDVI (Mynemi R.B. et al., 2002) are expected.

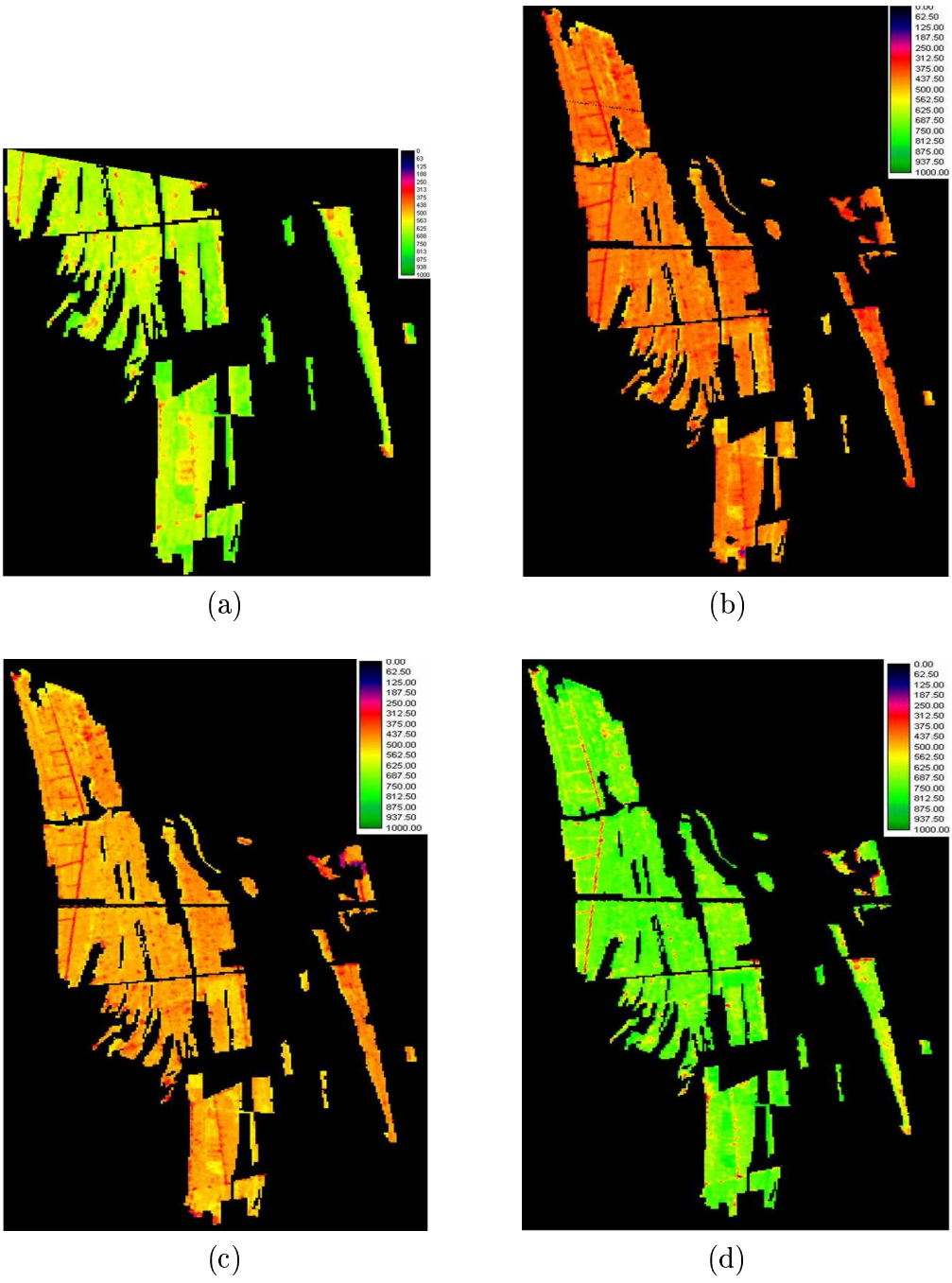

(a) (b)

(c) (d)

Figure 6.1: *NDVI images for the CHRIS-PROBA images taken into account in our work over the San Rossore Natural Park conifer forest. (a) is for June* 16*th 2003, (b) is for July* 25*th 2003, (c) is for September* 18*th 2003, (d) is for September* 8*th 2004.*

By means of CHRIS-PROBA RED and NIR[1] reflectances we are immedi-

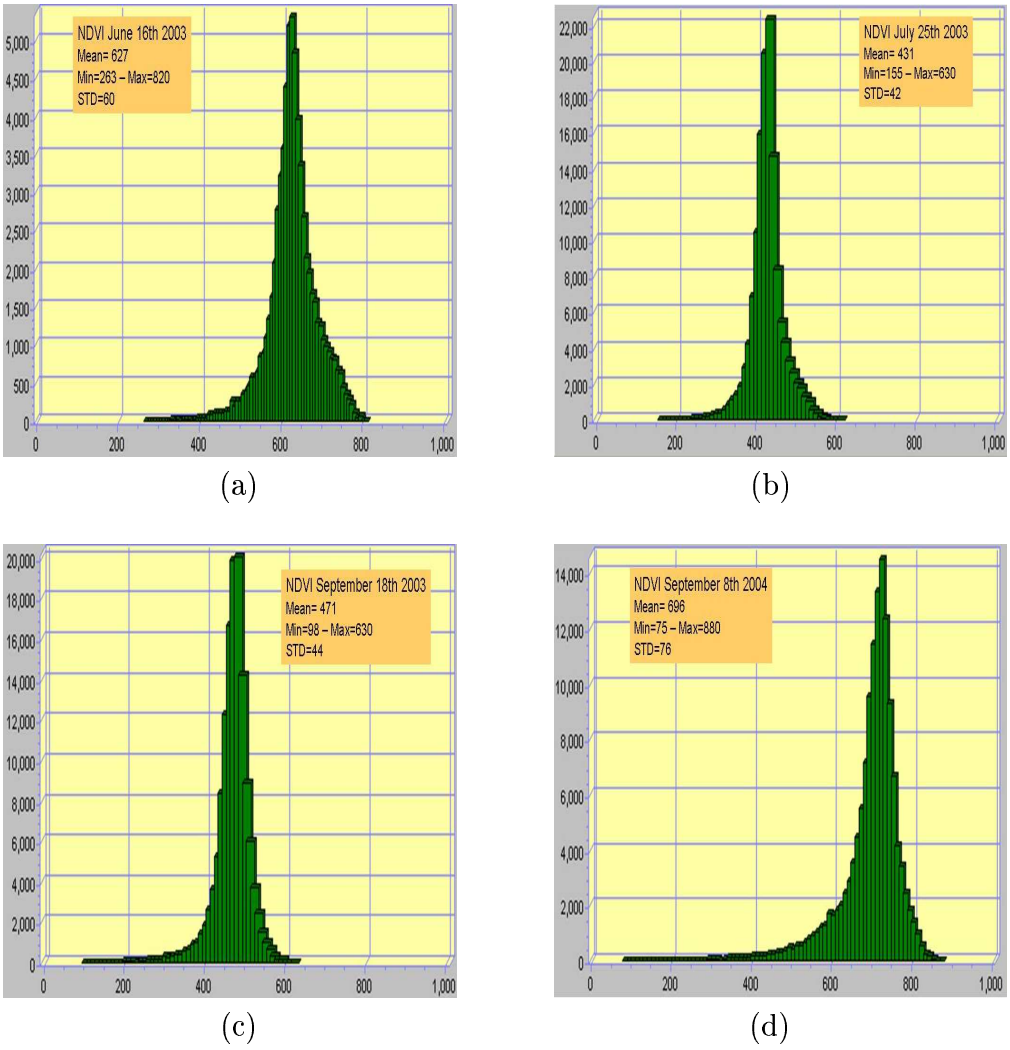

Figure 6.2: *Histograms obtained from a statistical analisysi on NDVI generated by RED and NIR CHRIS images: (a) June* 16*th 2003, (b) July* 25*th 2003, (c) September* 18*th 2003 nad (d) September* 8*th 2004.*

ately able to create NDVI maps. These maps are shown in figure (6.1), while in figure (6.2) the results of a simple statistical analysis (number of pixels versus NDVI values) on the some NDVI maps are presented. Histograms in figure (6.2) show systematically higher NDVI values on June 16th 2003

[1]RED is spectral channel centered at 630 nm, NIR is spectral channel centered at 870 nm.

(panel a) and September 8th 2004 (panel d) with respect to both the other images (panel b and c). This is true even for the standard deviations. Notice that panel (a) and (d) show very similar NDVI values, as well as panel (b) and (c). To better understand such a disagreement in NDVI values we can examine the original NIR CHRIS-PROBA images which are shown in figure (6.3). June 2003 and September 2004 data are very different from those on July and September 2003. As term of comparison we can take the sea pixels reflectance that should be almost costant, especially in the same season. We can note that the two images which look more realistic at a first glance (panels (b) and (c)) have indeed low, but non-zero, and nearly constant sea reflectance. On the contrary the sea region of the other two images exhibit nougth reflectances, looking like no-data pixels. The same is true even for RED spectral channel. This confirms that the disagreements between CHRIS-PROBA data could be given by bad sensor acquisitions and/or SIRA calibrations on both the images of June 16th 2003 and September 8th 2004. Moreover, to confirm these hypothesis, SIRA group is reprocessing all CHRIS-PROBA images with a new calibration algorithms release (Marcoionni P., 2005).

6.3 LAI results

As described in section (5.4) the chosen method for LAI retrieval is based on the soil line extraction from CHRIS-PROBA RED and NIR spectral channel. In this analysis we have followed two different approaches:

1) A different soil line has been extracted by each single CHRIS-PROBA acquisition and specifically used only for that image;

2) A single soil line is extracted by the merging of all the CHRIS acquisition and used for all the images.

Figure (6.4) and (6.5) show, respectively, LAI retrieved maps obtained from

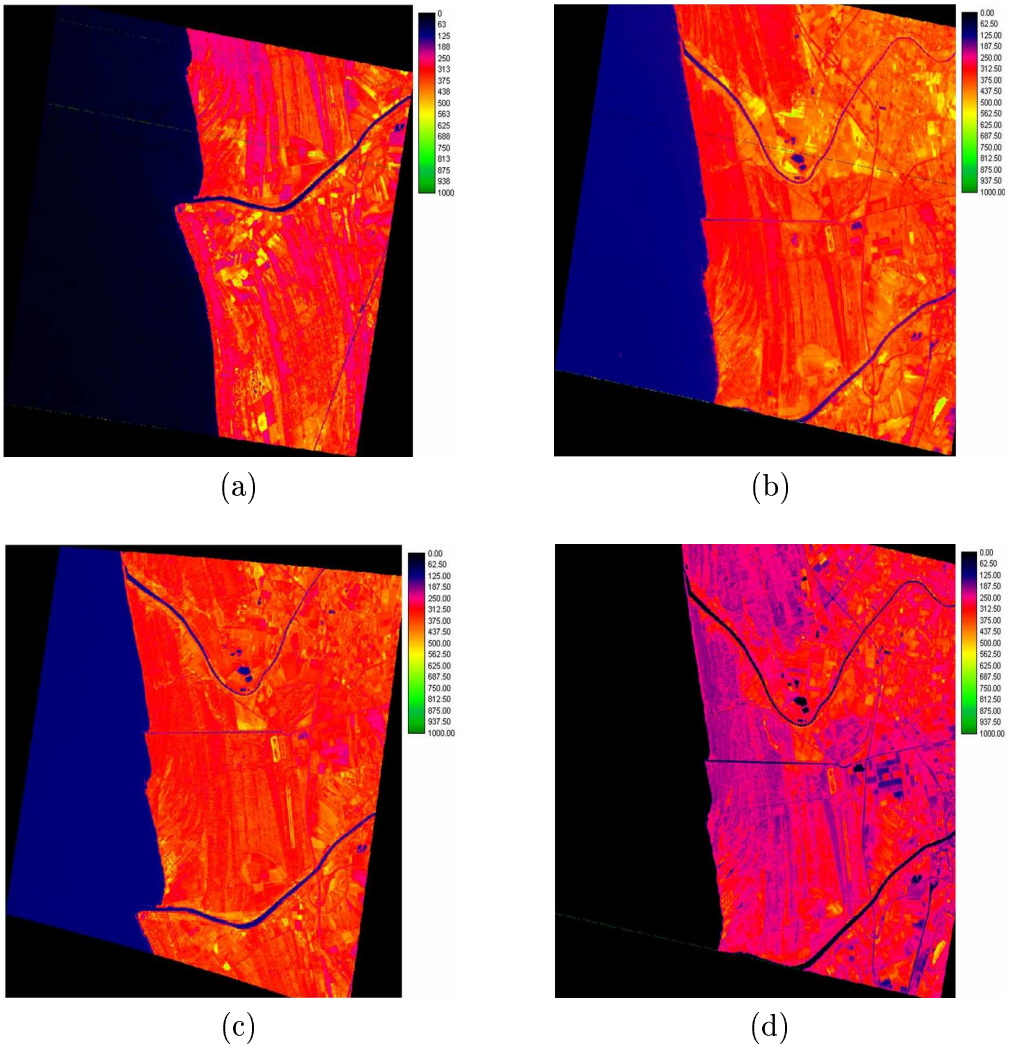

Figure 6.3: *CHRIS-PROBA NIR Spectral channel maps over the San Rossore Natural Park: (a) June* 16*th 2003, (b) July* 25*th 2003, (c) September* 18*th 2003, (d) September* 8*th 2004.*

the different soil lines approach and combined soil line method. Looking at the 2003 maps (panels a, b and c on both the figures) we can note relatively high changes in LAI values.

2003 summer was very hot and dry, with a long period without precipitation. From May to September only a few millimeters of rain felt and this probably caused a strong stress for the vegetation canopy. Examining the LAI maps

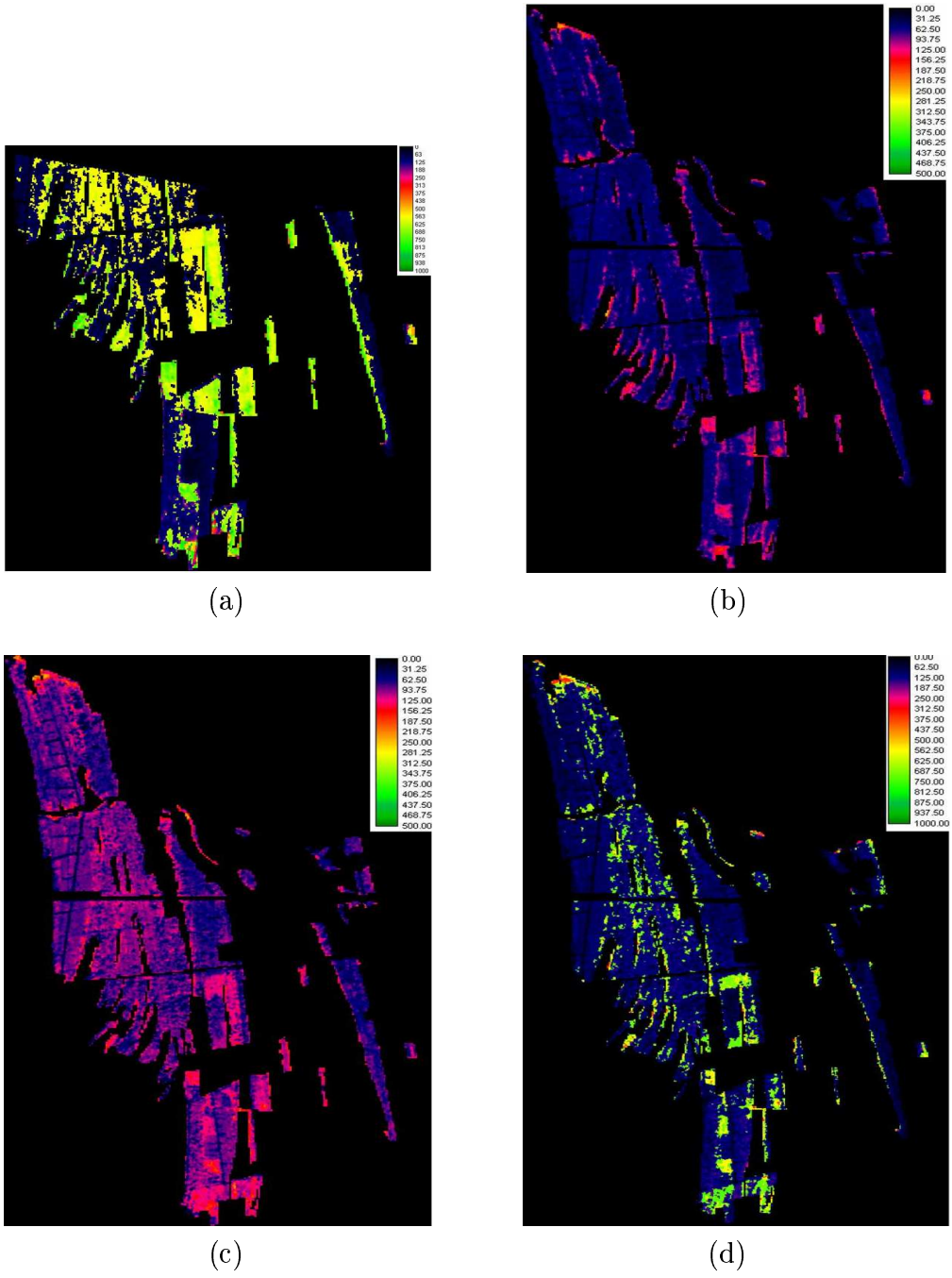

Figure 6.4: *LAI maps obtained from CHRIS-PROBA images over the San Rossore Natural Park, using for each image its specific soil line. (a) June* 16*th 2003, (b) July* 25*th 2003, (c) September* 18*th 2003, (d) September* 8*th 2004.*

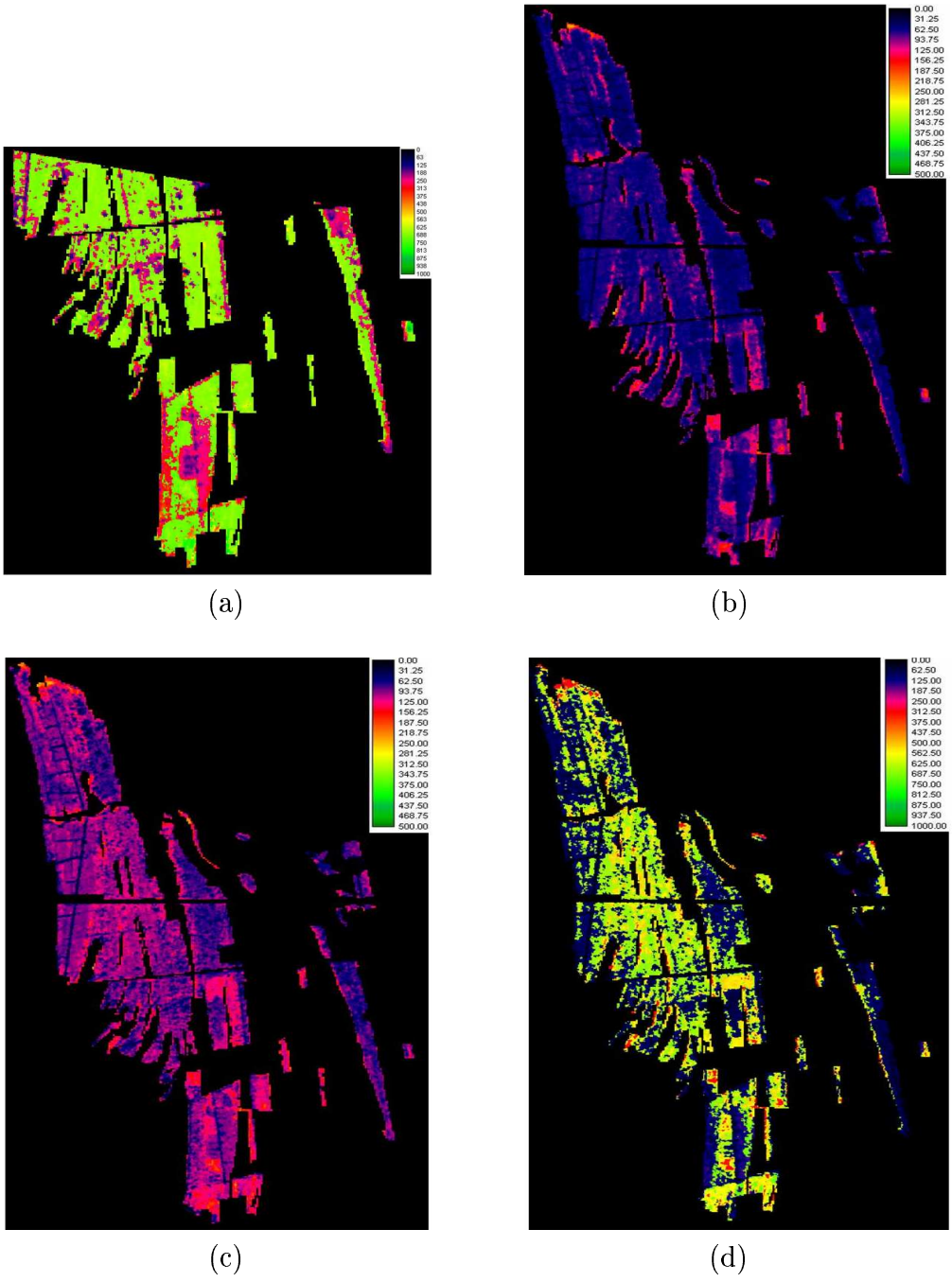

(a) (b)

(c) (d)

Figure 6.5: *LAI maps obtained from CHRIS images using a unique soil line. (a) June* 16*th 2003, (b) July* 25*th 2003, (c) September* 18*th 2003, (d) September* 8*th 2004.*

we can easily notice that June's LAI values are higher than July's LAI. Moreover, on September 9th 2003[2] 31mm of rain felt (data from LaMMA Meteorological data-base) and really the LAI values on September 18th 2003 are increased with respect to those of July's map.

As we have seen in section (5.2), from a theoretical point of view soil line should represent a given soil type in all its possibile conditions. So the soil line generated by all the CHRIS images is in principal the best choice. Therefore, the validation process explained below takes into account only LAI maps retrieved by the combined soil line (figure 6.5).

Validation and discussion of LAI results

As first step for the LAI validation process a simple statistical analysis has been applied to LAI retrieved maps, whose results are in figure (6.6). Panel a and d, respectively for June 16th 2003 and September 8th 2004, show very high standard deviation values, which clearly point out that bias and distortions in CHRIS reflectance data affects LAI retrieval processes.

As previously said the distribution of retrieved LAI with respect to the NDVI has to follow a logarithmic trend. In figure (6.7.a) is shown a scatter plot of NDVI-LAI on June 16th 2003: this image clearly produces a worse results and the same is true for September 8th 2004 LAI values. On the contrary, figure (6.7.b) shows an NDVI-LAI scatter plot where we can immediately note the well defined logarithmic shape. The same is valid for July 25th 2003 LAI maps. So, this is another confirmation that even though June 16th 2003 and September 8th 2004 LAI retrieved maps show plausible values, these are not meaningful to test our retrieval algorithms because of their probable bias.

Finally, retrieved LAI have to compared with in-situ measures of Leaf Area

[2]Precipitation occured just some days before the CHRIS-PROBA September 18th 2003 acquisition

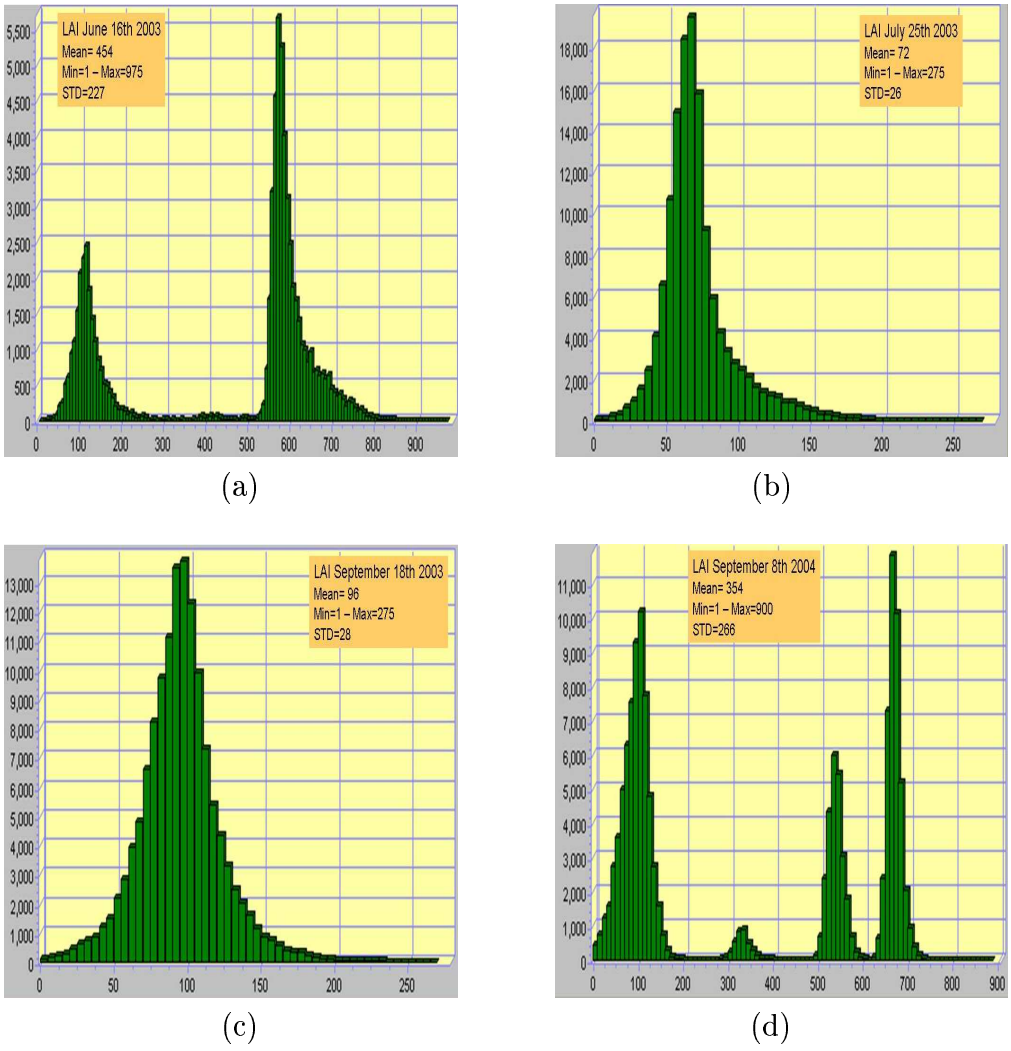

Figure 6.6: *Histograms obtained from a statistical analysis on LAI retrieved maps: (a) June* 16*th 2003, (b) July* 25*th 2003, (c) September* 18*th 2003 nad (d) September* 8*th 2004.*

Index. As described in chapter 4, some measurement campaigns have been carried out on San Rossore test site. Figure (6.8) summarizes LAI retrieved and ground based measured values. July and September 2003 scatter plot values and correlation factor ($R = 0.32$) immediately point out the poor accordance between measured and retrieved LAI. The former are sistematically higher than the latter. To understand such a disagreements two different fac-

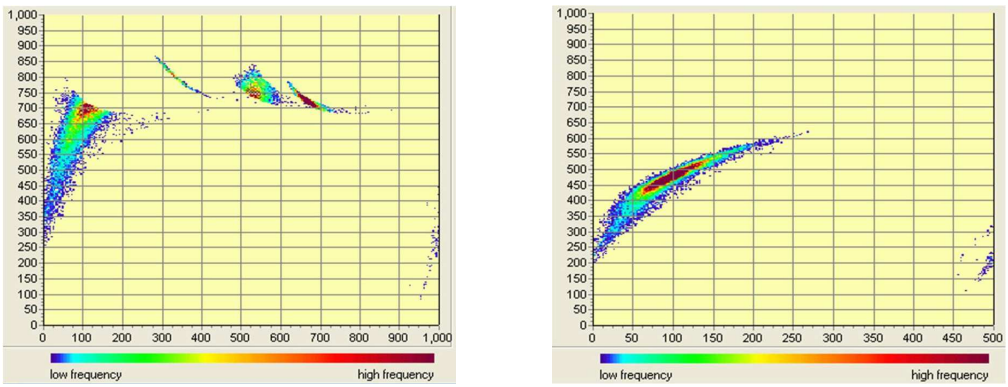

(a) (b)

Figure 6.7: *NDVI versus LAI values scatter plot: (a) September 8th 2004, (b) September 18th 2003. On September 2003 we obtain a well defined logarithmic trend. On the contrary September 2004 plot produce a worse result.*

	ground measured LAI		retrieved LAI			
ID	June 2003	Sept. 2004	June 2003	July 2003	Sept 2003	Sept 2004
2	4.2	3.7	/	0.7	1.0	6.0
3	4.3	4.0	/	0.8	1.0	6.0
4	4.5	/	5.7	0.6	0.9	5.0
5	3.7	3.8	5.7	0.5	0.9	6.0
6	4.8	/	6.0	0.7	0.9	6.8
7	4.2	4.5	5.8	1.5	1.5	6.0
8	4.6	3.9	/	0.7	1.4	5.4
9	4.2	/	/	0.7	1.1	5.0
10	5.1	/	/	1.4	1.4	7.0

Table 6.1: *Measured on San Rossore Natural Park and Retrieved from CHRIS reflectance data LAI values.*

tors have to be taken into account.

As seen in chapter 5 the difference between the measured soil line NIR axes interception and that extracted from the combination of all the images revals a probable offset in NIR CHRIS image which, obviously, affects the LAI retrieval process. Moreover, as seen in section 4.2, the ground-based LAI

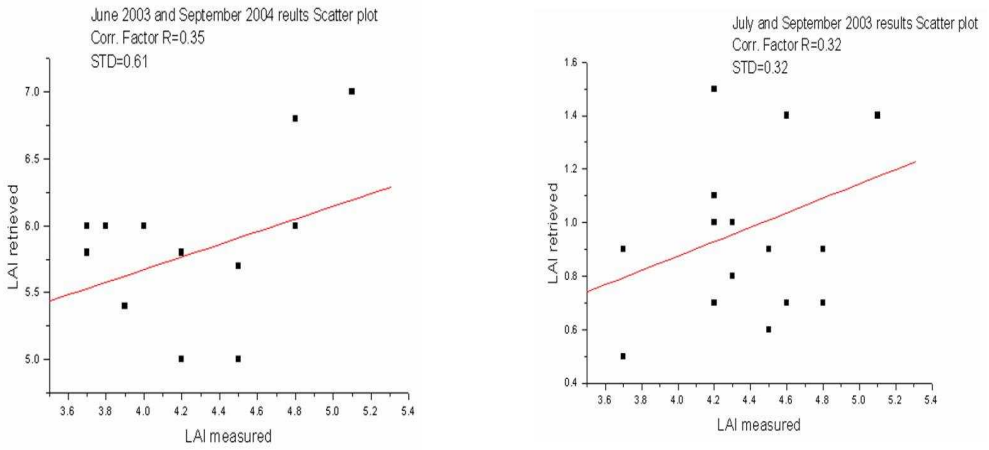

(a) (b)

Figure 6.8: *Retrieved versus measured LAI scatter plots: (a) June 16th 2003 and September 8th 2004, (b) July 25th 2003 and September 18th 2003.*

measurements were carried out by means of Li-Cor LAI2000 instrument. As suggested by Gower and Norman (Gower S.T. and Norman J.M., 1991) what we really measure with LICOR is the Plant Area Index (PAI) and not the Green Leaf Area Index. PAI is an overestimation of LAI because of trunks and branches radiation attenuation. Moreover, PAI shows a poor sensitivity in chlorophyll needles content fluctations that affect, and modify, reflectance spectra acquired by CHRIS sensor and therfore the retrieved LAI.

6.4 Soil Reflectance results

Once we have LAI estimations[3] we are able to evaluate also soil reflectances. From equation (5.8) we can find the f_s value. Substituting this into equation (5.6) and solving it for r_s we obtain the soil reflectance for all the spectral channel of interest. Figure (6.9) and (6.10) show, respectively, RED and NIR maps given by unique soil line processing. We immediately note that July and September 2003 maps (panel b and c respectively) give us the most

[3]Even in this case we take into account only results obtained using combined soil line

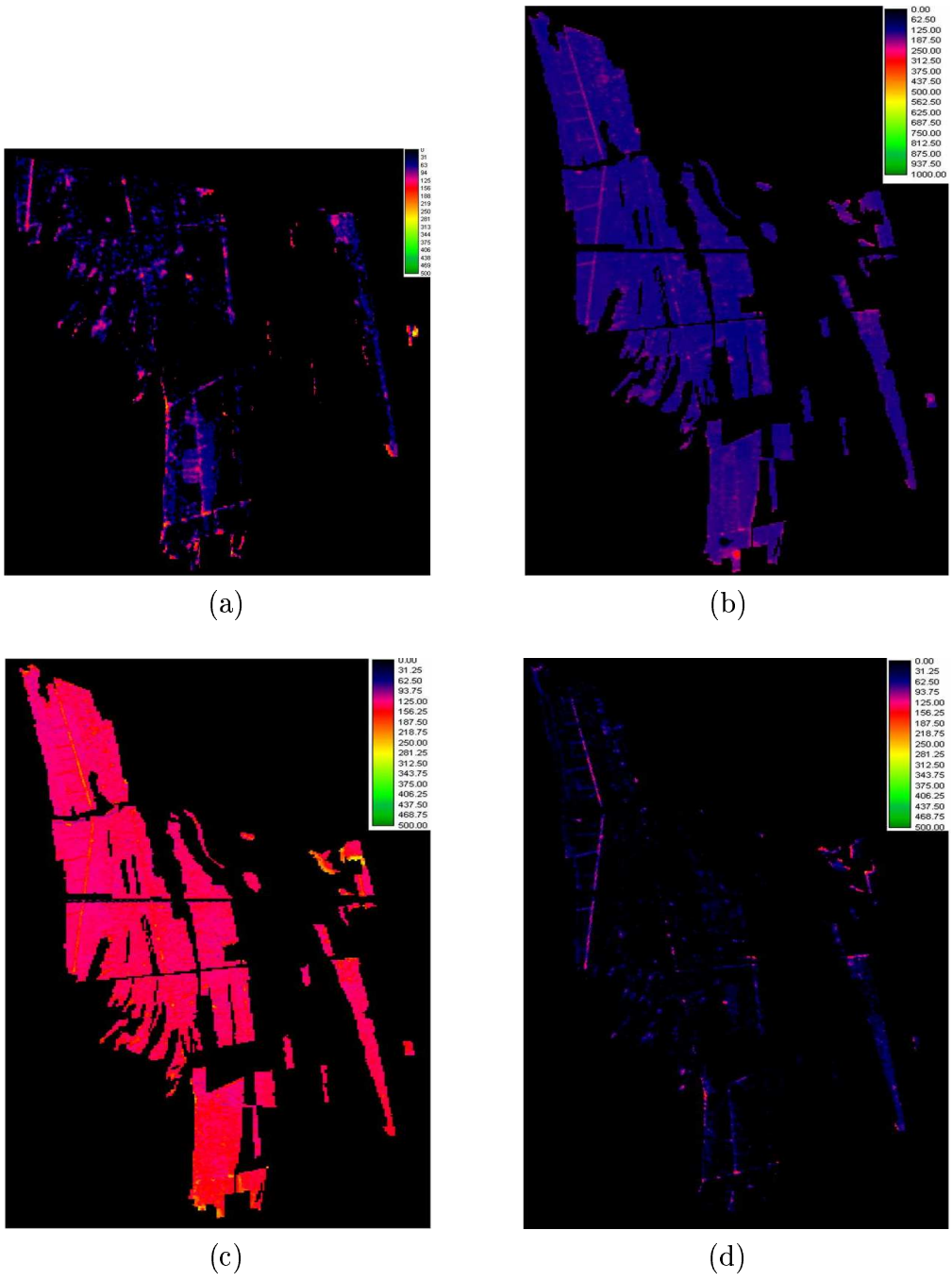

(a) (b)

(c) (d)

Figure 6.9: *CHRIS-PROBA RED Soil reflectance maps of the San Rossore Natural Park Pine Forest: (a) is for June* 16*th 2003, (b) is for July* 25*th 2003, (c) is for September* 18*th 2003, (d) is for September* 8*th 2004.*

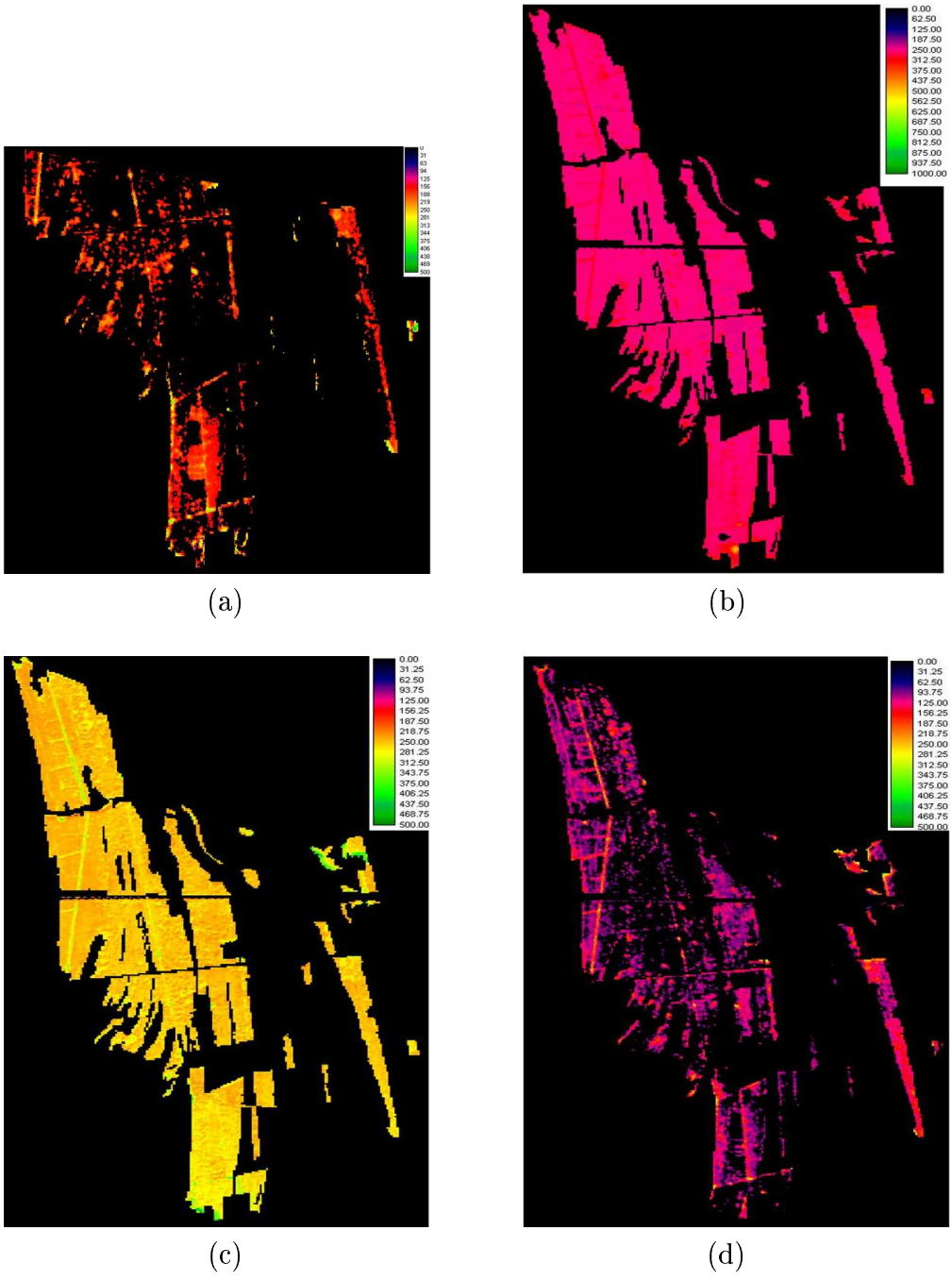

Figure 6.10: *CHRIS-PROBA RED Soil reflectance maps of the San Rossore Natural Park Pine Forest from unique soil line analysis: (a) is for June* 16*th 2003, (b) is for July* 25*th 2003, (c) is for September* 18*th 2003, (d) is for September* 8*th 2004.*

plausible results. Other images show that in practice soil reflectance can not be estimate at all. This is another clear indication that at least two CHRIS-PROBA TOC reflectance images are not good.

Combining soil reflectances retrieved for spectal channels 6 (Red), 3 (Green) and 1 (Blue) we should obtain a true color images of the San Rossore pine forest soil. Looking at RGB composition shown in figure (6.11.a) we can notice that there are a lot of blue pixels. Naturally soil can not be blue, but, from figure (6.11.b), it is evident that these bad coloured pixels match pixels with higher LAI values. This means that for high density vegetation we can not be sensitive to the very low reflectance signal of soil beneath the canopy. Then, algorithms are not able to extract the right soil reflectances for red and green spectral channel with a relative overestimation of the blue component. Regions with small LAI values show plausible soil colours and this is an indication that algorithms are physically correct.

6.5 FaPAR results

As described in the previous chapter, once LAI and soil reflectance have been retrieved, we are able to estimate Fraction of Photosynthetically Active Radiation absorbed by vegetation. Figure (5.15) shows FaPAR maps generated solving equation (5.17) using reflectances of all CHRIS spectral channels in the range between $400nm$ and $700nm$.

The statistical analysis applied to retrieved FaPAR point out high values of standard deviation (SD) for June 2003 and September 2004 images. On the contrary, for both the other maps we have found lower SD.

FaPAR ground-based measurements are not available but, as previously seen, a near-linear relation between FaPAR and NDVI is expected. Figure (6.13) shows the FaPAR, as calculate by the retrieved LAI and soil reflectances, versus NDVI for September 18th 2003 (panel a) and September 8th 2004

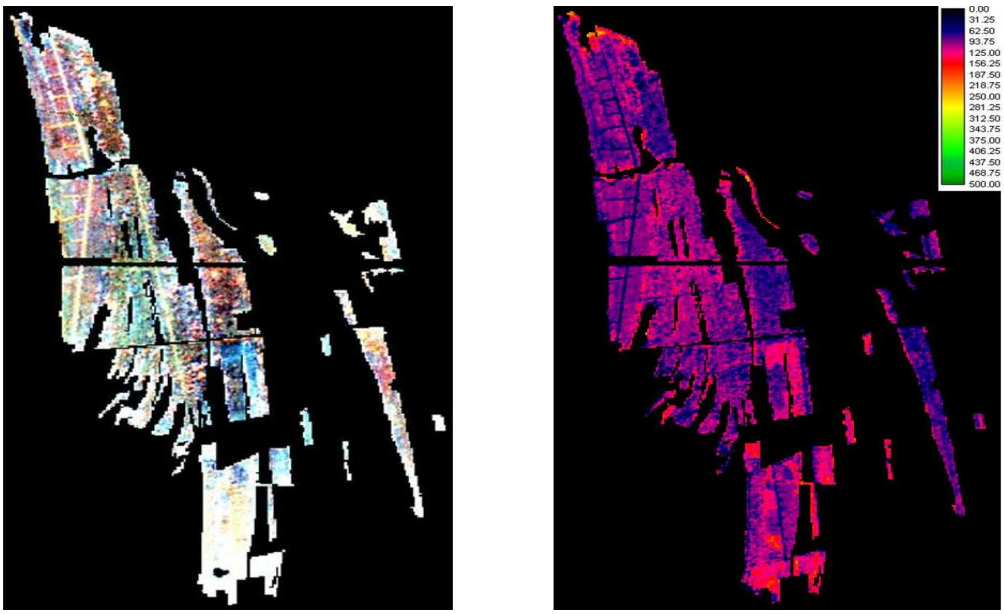

(a) (b)

Figure 6.11: *September 18th 2003 maps: (a) True colour images of San Rossore pine forest soil obtained form an RGB combination of soil reflectance maps retrieved for CHRIS spectral channels 6 (Red), 3 (Green) and 1 (Blue). (b) LAI retrieved maps*

(panel b). Figure (6.13.a) shows a distribution whose regression coefficient is $R = 0.92$. A similar distribution is followed by FaPAR versus NDVI scatter plot for July 25th 2003, but, in this case, regression coefficient is $R = 0.89$.

6.6 Conclusion and future plans

The algorithms developed in this work seem to be stable and robust. Retrieval processes are fast with a low cost in terms of computing time. Although the code is not yet optimised to process a full San Rossore pine forest image, of about 100 Mbyte, 20 seconds are needed. Optimizing retrieval chain, computing time could be reduced to an half.

By analysing the retrieved vegetation parameters maps we have verified the presence of bias and/or distortion in original CHRIS reflectance images. In

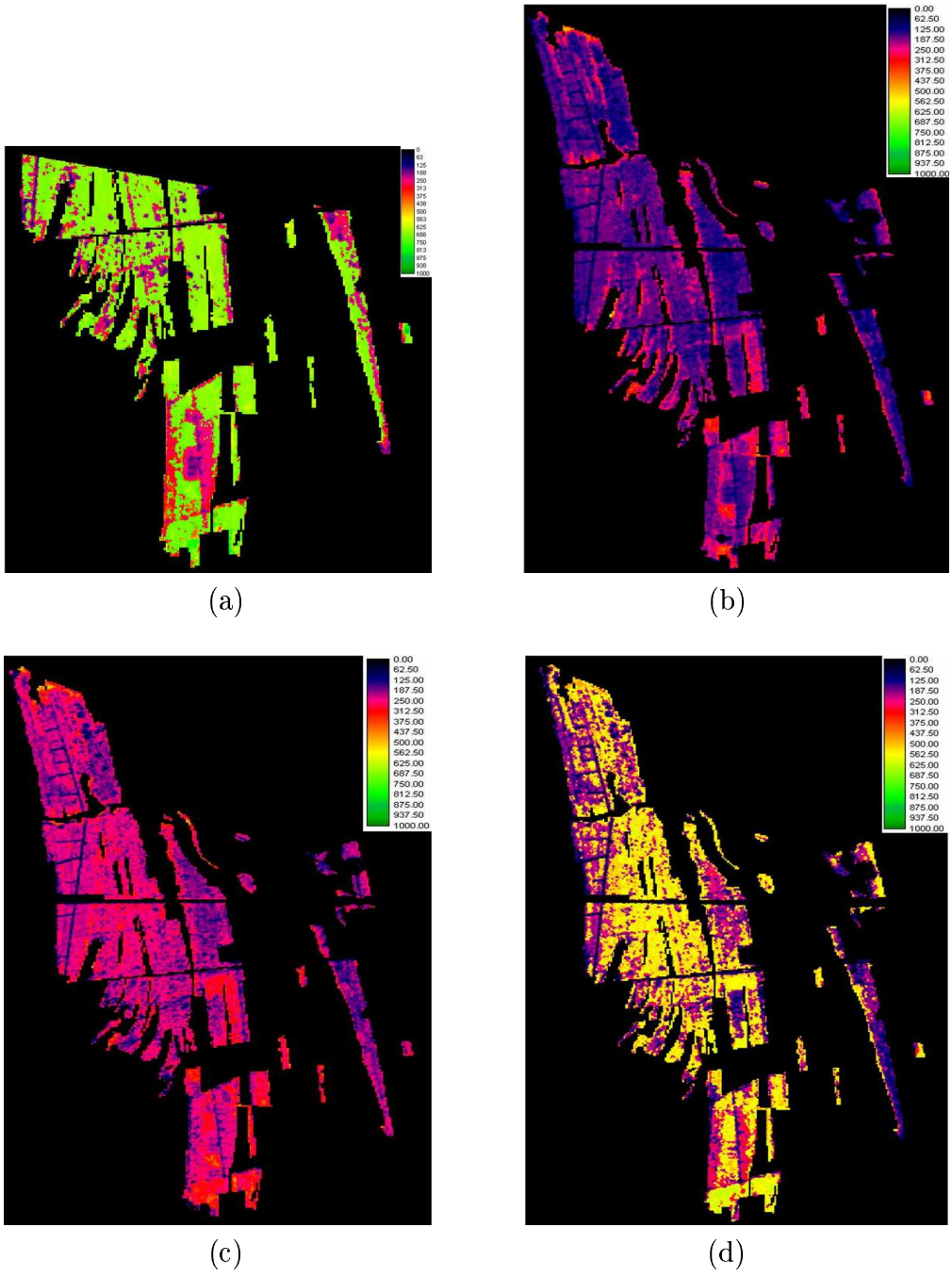

(a) (b)

(c) (d)

Figure 6.12: *FaPAR maps obtained from CHRIS-PROBA images over the San Rossore Natural Park, using for each image a different soil line. (a) is for June* 16*th 2003, (b) is for July* 25*th 2003, (c) is for September* 18*th 2003, (d) is for September* 8*th 2004.*

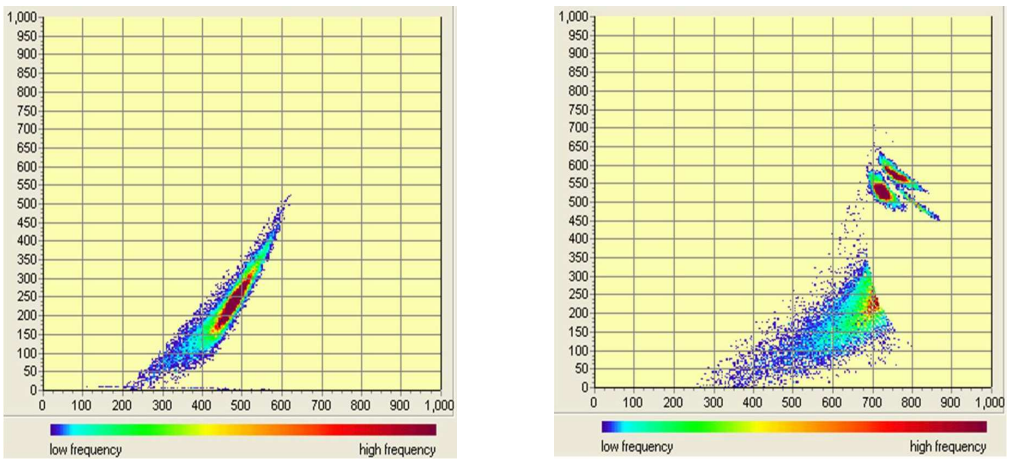

(a) (b)

Figure 6.13: *FaPAR versus NDVI scatter plots. (a) September 18th 2003, (b) September 8th 2003.*

particular most serious problems seem to come from the NIR data.

It is plausible to suppose that July 25th 2003 and September 18th 2003 are comparable in terms of calibratrion and atmospherical corrections, with only a probable offset affecting the reflectance data. Actually, vegetation retrieval maps show a correct statistical trend, as shown in figure (6.2) and (6.6) respectively for NDVI and LAI. Moreover, both NDVI versus LAI and FaPAR versus NDVI distributions, shown respectively in figure (6.7) and (6.13), agree with the theoretical expected trends.

Algorithms permit to estimate pine forest soil reflectances. RGB composition shown in figure (6.11.a), generated by retrieved channel 6 (Red), 3 (Green) and 1(Blue) soil reflectances, allows us to underline a physical limitation of the retrieval algorithms. In presence of dense vegetation canopy red and green soil reflectances signals are too low to make possible a correct estimation of soil reflectances. This limitation generate blue pixels in figure (6.11.a) but, to confirm the reliability of the algorithms, blue pixels match to pixels with higher LAI values.

Finally, the most serious problem comes from the LAI validation procedure, as shown in table (6.1) and figure (6.8 a and b). We certainly have an over estimation of LAI from the ground based measurements, as described in section 4.2. Moreover the difference between measured and extracted soil line NIR axes interception implies an offset in NIR CHRIS data that surely modify retrieved LAI values. It is important to test the algorithms on recalibrated CHRIS data and reflectances acquired by other sensors[4]. Major efforts to improve the retrieval procedure must be done in LAI validation, to estimate how much every single parameter affects the retrieval procedure. Then, measurement campaigns to study the effects of trunks and branches on the Li-Cor LAI2000 measurements as well as new data analysis to study the effects of the offset on the original CHRIS reflectance data once the recalibrated images will be available.

6.6.1 Future plans

Starting from this work many future activities can be planned. From a theoretical point of view the implementation of the four streams approximation of radiative transfer problem (described in Appendix A) is certainly an important improvement of the current algorithm. Moreover the development of a combinated soil-atmosphere forward model should be very important in the simulation of the signal acquired by an on-board satellite sensor. Model could be based on soil and vegetation properties treatment described in this work. Atmospheric multiple scattering could be founded on DISORT routine (Stamnes K. et al., 1988), combined with the MS-method approximation (Nakajima T. and Tanaka M., 1988) to solve the radiative transfer equation. Aerosol scattering phase function and coefficients could come from a database developed at the ISAC-CNR institute (Levoni C. et al., 1997). Absorp-

[4]Naturally, spectral and spatial resolution features required by the retrieval method, like a spatial resolution lower than 50×50 meter, have to be kept.

tion properties of atmospheric gas could be taken from the HITRAN data base (Lacis A.A. and Oinas V., 1991).

Laboratory and experimental measurements campaigns must be planned. Many efforts have to be devoted to LAI, soil reflectance and FaPAR in-situ measurements. These are needed to improve a most rigorous retrieved vegetation parameters validation process. Laboratory measurements on different vegetation canopies will give us the opportunity to apply this model to different biomes. Moreover could be interesting to analyse reflectance data acquired by different sensors in order to study the sensitivity of the algorithm.

Appendix A

Illumination and viewing directions inclusion

Once the two streams problem is solved, the inclusion of a direct illumination flux $F_{\hat{\mathbf{s}}}$ as well as of an upwelling flux $F_{\hat{\mathbf{v}}}$ toward an assigned viewing direction becomes a straightforward refinement. The direct illumination flux is considered suffering only an extinction process when propagates into the medium; on the contrary the $F_{\hat{\mathbf{v}}}$ flux rises from the contribution of all the other fluxes scattered into the viewing direction.

$$\begin{cases} \dfrac{dF_{\hat{\mathbf{s}}}}{d\tau} = -\hat{k}_{\hat{\mathbf{s}}} F_{\hat{\mathbf{s}}} \\ \dfrac{dF_{+}}{d\tau} = \hat{\sigma}_{\hat{\mathbf{s}}+} F_{\hat{\mathbf{s}}} - \hat{k}_{+} F_{+} + \hat{\sigma}_{-} F_{-} \\ \dfrac{dF_{-}}{d\tau} = \hat{\sigma}_{\hat{\mathbf{s}}-} F_{\hat{\mathbf{s}}} - \hat{\sigma}_{+} F_{+} + \hat{k}_{-} F_{-} \\ \dfrac{dF_{\hat{\mathbf{v}}}}{d\tau} = -\hat{\sigma}_{\hat{\mathbf{s}}} F_{\hat{\mathbf{s}}} + \hat{\sigma}_{\hat{\mathbf{v}}+} F_{+} + \hat{\sigma}_{\hat{\mathbf{v}}-} F_{-} + \hat{k}_{\hat{\mathbf{v}}} F_{\hat{\mathbf{v}}} \end{cases} \tag{1}$$

In this case the scattering matrix:

$$\mathbb{S} = \begin{pmatrix} -\hat{k}_{\hat{\mathbf{s}}} & 0 & 0 & 0 \\ \hat{\sigma}_{\hat{\mathbf{s}}+} & -\hat{k}_{+} & \hat{\sigma}_{-} & 0 \\ \hat{\sigma}_{\hat{\mathbf{s}}-} & -\hat{\sigma}_{+} & \hat{k}_{-} & 0 \\ \hat{\sigma}_{\hat{\mathbf{v}}} & \hat{\sigma}_{\hat{\mathbf{v}}+} & \hat{\sigma}_{\hat{\mathbf{v}}-} & \hat{k}_{\hat{\mathbf{v}}} \end{pmatrix} \tag{2}$$

has four eigenvalues, two of them identical to those of the two streams matrix:

$$\begin{aligned}
\hat{\alpha}_0 &= -\hat{k}_{\hat{\mathbf{s}}} \\
\hat{\alpha}_1 &= \frac{(\hat{k}_+ - \hat{k}_-) - \sqrt{(\hat{k}_+ + \hat{k}_-)^2 - 4\hat{\sigma}_+\hat{\sigma}_-}}{2} \\
\hat{\alpha}_2 &= \frac{(\hat{k}_+ - \hat{k}_-) + \sqrt{(\hat{k}_+ + \hat{k}_-)^2 - 4\hat{\sigma}_+\hat{\sigma}_-}}{2} \\
\hat{\alpha}_3 &= \hat{k}_{\hat{\mathbf{v}}}
\end{aligned} \tag{3}$$

The solution for the direct illumination radiation is immediately found:

$$F_{\hat{\mathbf{s}}}(\tau) = F_0 e^{-\hat{k}_{\hat{\mathbf{s}}}\tau} \tag{4}$$

As concerns the diffuse fluxes we search again for solutions of the form:

$$F_{\pm}(\tau) = \sum_{i=0}^{3} c_{i\pm} e^{\hat{\alpha}_i \tau} \tag{5}$$

All the coefficients for each exponential term must vanish separately once the expressions 5 are introduced into the corresponding differential equation of the system 1, with $F_{\hat{\mathbf{s}}}$ given by 4. Vanishing all the coefficients for the term $e^{-\hat{k}_{\hat{\mathbf{s}}}\tau}$ we get the two coupled equation:

$$-\hat{k}_{\hat{\mathbf{s}}} c_{0\pm} = \hat{\sigma}_{\hat{\mathbf{s}}\pm} F_0 \mp \hat{k}_{\pm} c_{0\pm} \pm \hat{\sigma}_{\mp} c_{0\mp} \tag{6}$$

whose solutions are:

$$c_{0\pm} = \frac{\pm\hat{\sigma}_{\mp}\hat{\sigma}_{\hat{\mathbf{s}}\mp} - (\hat{k}_{\hat{\mathbf{s}}} \pm \hat{k}_{\mp})}{(\hat{k}_{\hat{\mathbf{s}}} \mp \hat{k}_{\pm})(\hat{k}_{\hat{\mathbf{s}}} \pm \hat{k}_{\mp}) + \hat{\sigma}_+\hat{\sigma}_-} F_0 \tag{7}$$

Thus the functions:

$$\tilde{F}_{\pm}(\tau) \equiv F_{\pm}(\tau) - c_{0\pm} e^{-\hat{k}_{\hat{\mathbf{s}}}\tau} \tag{8}$$

satisfy two coupled differential equations which exactly correspond to those of the two streams problem. Once the expressions for the diffuse radiation

$F_\pm$ are known, they can be introduced in the fourth differential equation together with 4. In this way the expression for $F_{\hat{\mathbf{v}}}$, whose general form is of the type 5, may be easily determined.

Let us treat in more details the special case of a medium with an underlying Lambertian surface with reflectance r_s. If the diffuse incident radiation at $\tau = 0$ is a known fraction p of the direct radiation $F_{\hat{\mathbf{s}}}(0) = F_0$, the boundary conditions read:

$$\begin{aligned} F_{\hat{\mathbf{s}}}(0) &= F_0 \\ F_+(0) &= pF_0 \\ F_-(T) + F_{\hat{\mathbf{v}}}(T) &= r_s \left[F_{\hat{\mathbf{s}}}(T) + F_+(T)\right] \end{aligned} \tag{9}$$

These imply for the functions $\tilde{F}_\pm$ of 8 the following boundary conditions:

$$\begin{aligned} \tilde{F}_+(0) &\equiv \tilde{F}_0 = pF_0 - c_{0+} \\ \tilde{F}_-(T) &= r_s \tilde{F}_+(T) + \left[(c_{0+} + F_0)\, r_s e^{-\hat{k}_{\hat{\mathbf{s}}} T} - F_{\hat{\mathbf{v}}}(T)\right] \end{aligned} \tag{10}$$

which differ with respect to the ones of the two streams problem we have already solved by the additional term:

$$G \equiv \left[(c_{0+} + F_0)\, r_s e^{-\hat{k}_{\hat{\mathbf{s}}} T} - F_{\hat{\mathbf{v}}}(T)\right] \tag{11}$$

The searched solutions are:

$$\begin{aligned} \tilde{F}_+(\tau) &= \frac{\left[(r_2 - r_s)\tilde{F}_0 e^{\hat{\alpha}_2 T} - G\right] e^{\hat{\alpha}_1 \tau} + \left[G - (r_1 - r_s)\tilde{F}_0 e^{\hat{\alpha}_1 T}\right] e^{\hat{\alpha}_2 \tau}}{(r_2 - r_s)e^{\hat{\alpha}_2 T} - (r_1 - r_s)e^{\hat{\alpha}_1 T}} \\ \tilde{F}_-(\tau) &= \frac{\left[(r_2 - r_s)\tilde{F}_0 e^{\hat{\alpha}_2 T} - G\right] r_1 e^{\hat{\alpha}_1 \tau} + \left[G - (r_1 - r_s)\tilde{F}_0 e^{\hat{\alpha}_1 T}\right] r_2 e^{\hat{\alpha}_2 \tau}}{(r_2 - r_s)e^{\hat{\alpha}_2 T} - (r_1 - r_s)e^{\hat{\alpha}_1 T}} \end{aligned} \tag{12}$$

From these expressions the diffuse radiation fluxes $F_\pm$ can be immediately derived by 8. Finally substituting the $F_\pm$ and the $F_{\hat{\mathbf{s}}}$ expressions in the fourth differential equation of 1 we get the four coefficients c_i for $F_{\hat{\mathbf{v}}}$:

$$F_{\hat{\mathbf{v}}}(\tau) = \sum_{i=0}^{3} c_i e^{\hat{\alpha}_i \tau} \tag{13}$$

In particular the first three coefficients are determined by vanishing the corresponding exponential terms separately and the fourth by imposing the boundary condition 9 at $\tau = T$:

$$
\begin{aligned}
c_0 &= \frac{\hat{\sigma}_{\hat{\mathbf{s}}} F_0 - \hat{\sigma}_{\hat{\mathbf{v}}+} c_{0+} - \hat{\sigma}_{\hat{\mathbf{v}}-} c_{0-}}{\hat{k}_{\hat{\mathbf{s}}}} \\
c_1 &= \frac{(r_2 - r_s)\tilde{F}_0 e^{\hat{\alpha}_2 T} - G}{\hat{\alpha}_1 \left[(r_2 - r_s)e^{\hat{\alpha}_2 T} - (r_1 - r_s)e^{\hat{\alpha}_1 T}\right]} (\hat{\sigma}_{\hat{\mathbf{v}}+} + r_1 \hat{\sigma}_{\hat{\mathbf{v}}-}) \\
c_2 &= \frac{G - (r_1 - r_s)\tilde{F}_0 e^{\hat{\alpha}_1 T}}{\hat{\alpha}_2 \left[(r_2 - r_s)e^{\hat{\alpha}_2 T} - (r_1 - r_s)e^{\hat{\alpha}_1 T}\right]} (\hat{\sigma}_{\hat{\mathbf{v}}+} + r_2 \hat{\sigma}_{\hat{\mathbf{v}}-}) \\
c_3 &= \left[(r_s F_0 + r_s c_{0+} - c_{0-})e^{-\hat{k}_{\hat{\mathbf{s}}} T} + r_s \tilde{F}_+(T) - \tilde{F}_-(T)\right] e^{-\hat{k}_{\hat{\mathbf{v}}} T}
\end{aligned}
\tag{14}
$$

where $c_{0\pm}$ are given by 7, r_i by 2.37, $\hat{\alpha}_i$ by 3 and $\tilde{F}_0$ by 10.

Appendix B

Soil line extraction using CHRIS spectral channel 17 centered at 907.7 nm (Channel 17)

From a theoretical point of view, in the soil line extraction process, the best choice of NIR CHRIS spectral channel should be channel 17 centered at 907 nm. NIR versus RED scatter plots generated by all the available CHRIS images are shown in figure (14) where every single soil line are traced. In table (2) are summarized constant parameters a and b. The best accordance

Image	a	b
june 16 2003	0.77	0.165
july 25 2003	1.0	0.2
september 18 2003	1.0	0.25
september 8 2004	0.66	0.1

Table 2: *Constant parameters for soil line obtained from CHRIS-PROBA RED and NIR images.*

is between images of July 25 and September 18 which give the same value for a and a 20% relative difference for b coefficient.

As seen in chapter 5, if all the used images are comparable in terms of calibration and atmospherical correction a better defined soil line is expected by their merging.

Unfortunately, the probable miscalibration of the CHRIS channel 15 remarked in chapter 6 is present also for spectral channel 17. In this case the effects of bad calibration on soil line extraction process are even larger. Actually the merging of single scatter plots shown in figure (14) clearly produces a worst result, as visible in figure (16), and the soil line can not be

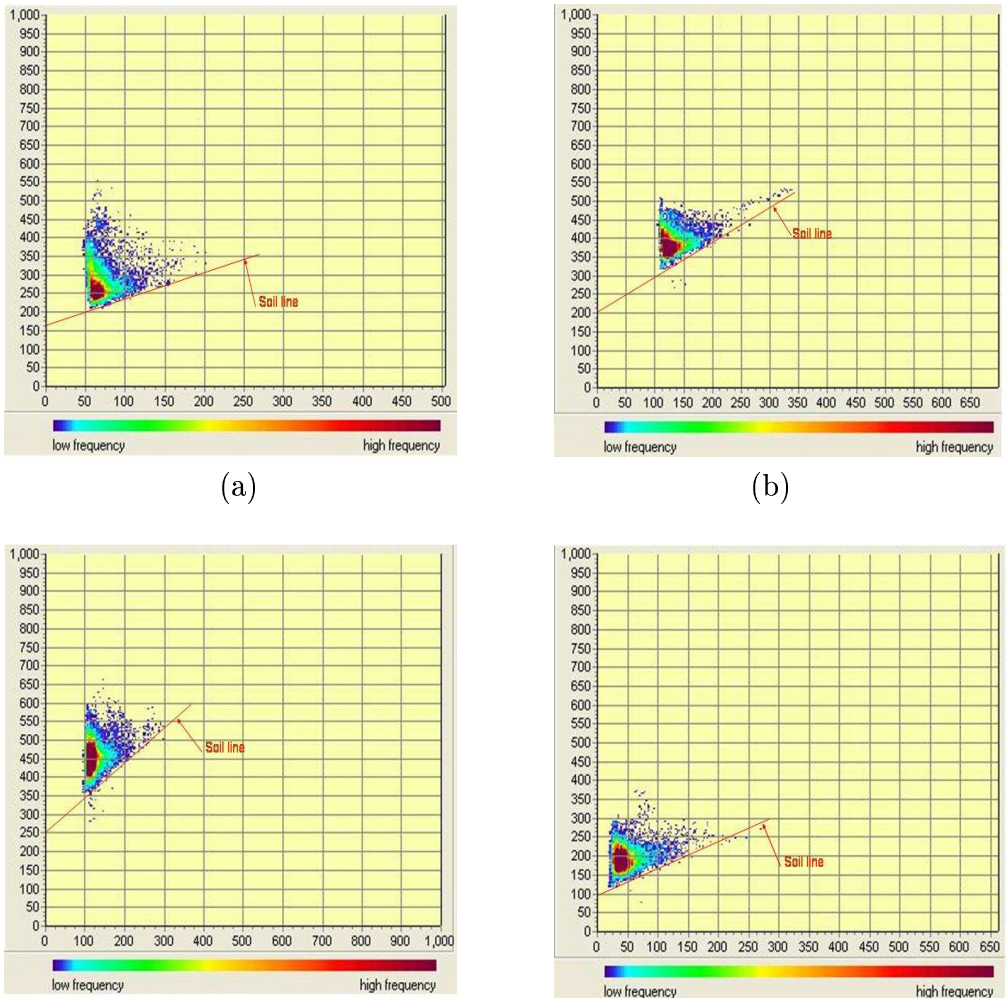

Figure 14: *Scatter plot for the four CHRIS-PROBA images analized in our work over the San Rossore Natural Park. (a) June* 16*th 2003, (b) July* 25*th 2003, (c) September* 18*th 2003, (d) September* 8*th 2004.*

traced at all. This represents a clear indication that some mismatch accurred during the CHRIS data calibration.

In order to single out the most reliable images we have compared each NIR-RED scatter plots with the others. As shown in figure (17.a) the reflectance data acquired on June 16th 2003 and September 8th 2004 do not match with the others as well as between themself. On the contrary, as visible in figure

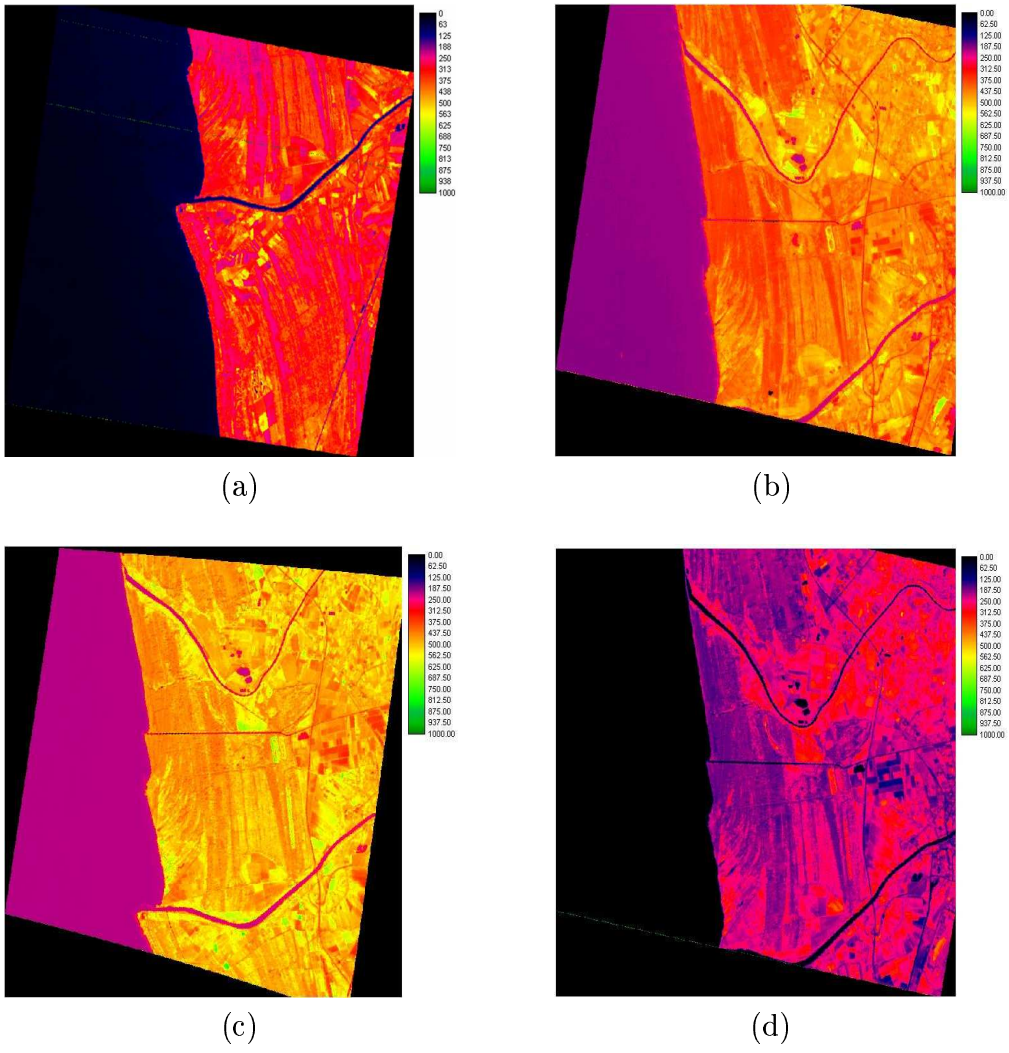

Figure 15: *CHRIS-PROBA NIR Spectral channel maps over the San Rossore Natural Park: (a) June* 16*th 2003, (b) July* 25*th 2003, (c) September* 18*th 2003, (d) September* 8*th 2004.*

(17.b) data on July 25th 2003 and Septermber 18th 2003 are comparable and give a well defined soil line. In addition in this case the slope a turns out comparable with the measured soil line angular coeffcient. On the contrary b constant is five times than measured b coefficient.

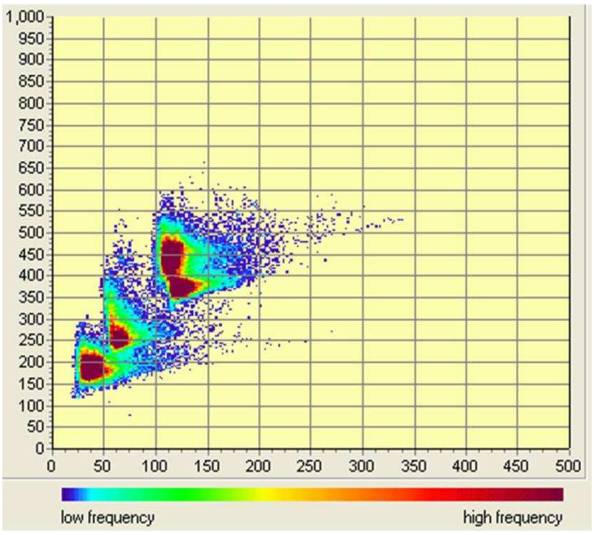

Figure 16: *Combinated scatter plot of all the CHRIS images used.*

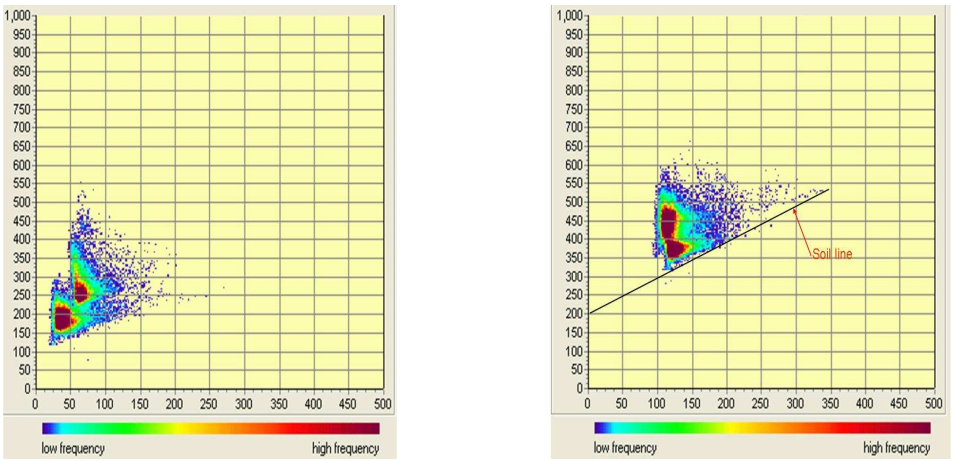

(a) (b)

Figure 17: *figure (a) shows the NIR vs RED scatter plot of June 16th 2003 and September 8th 2004. (b) is the NIR vs RED scatter plot of July 25th 2003 and Septermber 18th 2003 where a well defined soil line is traced with parameters* $a = 1.0$ *and* $b = 0.2$.

References

ASTER Science Team, 2005: ASTER Instrument Characteristics, *Jet Propulsion Laboratory*, http://asterweb.jpl.nasa.gov/instruments/character.htm

Barducci A., Guzzi D.,Marcoionni P., Pippi I., Selva M., 2005: CHRIS-PROBA on San Rossore Test Site: CORSARI Technical Guide, *http://www.ifac.cnr.it*

Barducci A., Guzzi D., Marcoionni P., Pippi I., 2002: Atmospheric effects on hyperspectral data acquired with aerospace imaging spectrometers *Optics in atmospheric propagation and adaptive system V edited by A. Kohle, J.D. Gonglewski, SPIE*, **4884,** pp 1-9;

Benedetti R., Chiesi M., **Cristofori S.**, Marcoionni P., Maselli F., Pippi I., 2005: Testing out the leaf area index extraction from CHRIS-PROBA images, *Riv. Ital. Tel.*, **accepted** ;

Berk A., et al., 2000: MODTRAN 4 user's manual *Air Force Research Laboratory*;

Chandrasekhar S., 1960: Radiative transfer; Dover Publications INC., New York, pp 393;

Chen J.M., Rich, P.M., Gower S.T., Norman J.M., Plummer S., 1997: Leaf area index of boreal forests: Theory, techniques, and measurements, *Jour. Geo. Res.*, **102,** pp 29429-29443;

Chen X., Vierling L., Rowell E., DeFelice T., 2004: Using lidar and effective LAI data to evaluate IKONOS and LandSat 7 ETM+ vegetation cover estimates in a ponderosa pine forest, *Rem. Sens. Env.*, **91 ,** pp 14-26;

CHRIS-PROBA official web site, 2005;*http://www.chris-proba.org.uk*

Gobron N., Pinty B., Verstraete M.M., Govaerts Y., 1997: A semidiscrete model for scattering of light by vegetation, *Jour. Geo. Res.*, **102,** pp 9431-9446;

Gower S.T. and Norman J.M., 1991: Rapid estimation of leaf area index in conifer and broad-leaf plantation, *Ecology*, **72,** pp 1896-1900;

Hatchell D.C., 1999: Technical Guide 3rd Edition *Analytical Spectral Device, Inc.*

Hosgood B., et al., 2003: The JRC leaf optical properties experiments (LOPEX 03), *JRC report*;

Hu b., Miller J.R, Jing M.C., Hollinger A., 2004: Retrieval of the canopy leaf area index in the BOREAD flux tower sites using linear spectral mixture analysis *Rem. Sens. Envi.* **89,**pp 176-188;

Kaufman Y.J. and Gao B., 1992: Remote sensing of water vapor in the near IR from EOS/MODIS, IEEE Geo. Rem. Ses. **30,** pp 871-884;

King M.D., Kaufman Y.J., Tanre D., Nakajima T., 1999: Remote sensing of tropospheric aerosol from space: past, present and future, *Bullet. Meteo. Socie.*, **80,**pp2229-2259;

King M.D., et al, 2003: Cloud and aerosol properties, precipitable water and profiles of temperature and water vapor from MODIS IEEE Geo. Rem. Ses. **41,** pp 442-458;

Knyazikhin Y., Martonchik J.V., Myneni R.B., Diner D.J., Running S.W., 1998: Synergistic algorithm for estimating vegetation canopy leaf area index and fraction of absorbed photosynthetically active radiation from MODIS and MISR data, *Jour. Geo. Res.*, **103,** pp 32257-32275;

Knyazikhin Y., Glassy J., Privette J.L., Tian Y., Lotsch A., Zhang Y., Wang Y., Morisette J.T., Votava P., Mynemi R.B., Nemani R.R., Running S.W., 1999: MODIS leaf area index (LAI) and fraction of photosynthetically active radiation absorbed by vegetation (FPAR) product (MOD15) Algorithm Theoretical Basis Document, *http://eospso.gsfc.nasa.gov/atbd/modistables.html*;

Kuusk, A. and Nilson T., 2000: A Directional Multispectral Forest Reflectance Model, *Rem. Sens. Env.*, **72,** pp 244-252;

Lacis A.A. and Oinas V., 1991: A description of the Correlated k distribution method for modeling nongray gaseous absorption, thermal emission, and multiple scattering in vertically inhomogemeous atmospheres, *Jour. Geoph. Research*, **96,**pp 9027-9063;

LandSat Science Team, 2005: LandSat Thecnical Guide, *U.S. Geological Survey*, http://edc.usgs.gov/products/satellite/landsat7.htm

Levoni C., Cervino M., Guzzi R., Torricella F., 1997: Atmospherical aerosol optical properties: a database of radiative characteristics for different components and classes, *Appl. Opt.*, **36,** pp 8031-8041;

LI-COR team, 2005: LAI-2000 Plant canopy analyzer *LI-COR Ltd*;

Liou K.N., 1980: An introduction to atmospheric radiation *Academic Press, LTD*;

Marcoionni P., 2005: Personal Communication;

Menenti M., Maselli F., Chiesi M., Benedetti R., **Cristofori S.**, Guzzi D., Magnani F., Raddi S., Maffei C., 2004: Multi-angular hyperspectral observations of Mediterranean forest with PROBA-CHRIS, *Imagery Spectrometry X - SPIE Proceedings*, **5546,** pp 204-212;

Mynemi R.B. and Williams D.L., 1994: On the relationship between FaPAR and NDVI, *Rem. Sens. Env.*, **49,** pp 200-211;

Myneni R.B., et al., 2002: Global products of vegetation leaf area and fraction absorbed PAR from year one of MODIS data, *Rem. Sens. Env.*, **83,** pp 214-231;

Nakajima T. and Tanaka M., 1988: Algorithms for radiative intensity calculation in moderate thick atmopsheres using a truncation approximation, *J. Qunt. Spectr. Radiat. Transfer*, **40,** pp 51-69;

Price J.C., 1990: On the information content of soil reflectance spectra, *Rem. Sens. Env.*, **33,** pp 113-121;

Price J.C., 1993: Estimating leaf area index from satellite data, *IEEE Trans. Geo. Rem. Ses.*, **31,** pp 727-734;

Price J.C. and Bausch W.C., 1995:Leaf Area Index Estimation from visible and near-infrared reflectance Data, *Rem. Sens. Env.*, **52,** pp 55-65;

SPOT Science Team, 2005: SPOT Payload Technical Information *www.spotimage.fr*

Stamnes K., Tsay S.C., Winscombe W., Jayaweera K., 1988: Numerically stable algorithm for discrete-ordinate-method radiative transfer in multiple scattering and emitting layered media. *Appl. Opt.*, **27,** pp 2502-2509;

Wallace J.M. and Hobbs P.V., 1977: Atmospheric science: An introductory survey *Academic Press, LTD*;

Wang Y. et al., 2004: Evaluation of the MODIS LAI algorithm at a coniferous forest site in Finlad, *Rem. Sens. Env.*, **91,** pp 114-127;

Zarco-Tejada P.J. et al., 2004: Needle chlorophyll content estimation through model inversion using hyperspectral data from boreal conifer forest canopies, *Rem. Sens. Env.*, **89,** pp 189-199;

Acknowledgement

First of all, I would like to thank Prof. Fabio Del Frate, Prof. Domenico Solimini and all the DISP staff to give me the possibility to attend the Geoinformation PhD course.
I would like to thank Prof. Massimo Menenti and Dr. Fabio Maselli that give me the opportunity to realize this work.
Dr. Paolo Marcoionni, Dr. Ivan Pippi and Dr. Donatella Guzzi (IFAC-CNR) for the provided CHRIS atmospherically correct images.
I would like to thank Dr. Alberto Ortolani, Ing. Carlo Brandini, Ing. Andrea Antonini, Dr. Samantha Melani, Dr. Andrea Orlandi, Dr. Graziano Giuliani, Dr. Antonietta Del Piccolo, Dr. Lorenzo Bottai and all the LaMMA staff for their support and friendship.
A particular thank to Dr. Marta Chiesi and Dr. Maurizio Pieri for their friendship and scientific support in the San Rossore measurements campaigns.
A very special thank to Dr. Riccardo Benedetti for his great scientific support and friendship, basic for the thesis realization.

Finally, a very special and great thank to my wife Maria who support and believe in me.